ORIGINAL ARTICLE

Shaking table test and numerical analyses of a full scale three-leaf masonry wall

Francesco Di Michele[1] · **Enrico Spacone**[1] · **Guido Camata**[1] · **Giuseppe Brando**[1] · **Anastasios Sextos**[2,5] · **Adam Crewe**[2] · **George Mylonakis**[2,4] · **Matt Diez**[2] · **Luiza Dihoru**[2] · **Humberto Varum**[3]

Abstract

This paper discusses the main results of a full-scale shaking table test campaign carried out under the auspices of the EU funded research project SERA, whose objective is to investigate the seismic performance of three-leaf masonry walls with weak lime-mortar joints. These masonry walls are widely found in seismic prone regions in the Mediterranean area, thus assessing their behaviour under dynamic actions is an important pre-requisite for the seismic vulnerability evaluation of a plethora of historical centres. The first part of the paper presents a preliminary study on the mechanical properties of the wall component materials that was carried out through an *ad-hoc* experimental campaign. The outcomes are of particular interest for the characterization of the mortar and of the infill materials, that were designed to reproduce the low strength that is typically found in old masonry buildings. The design of the masonry wall that was tested and the test set-up are presented next. The applied loading protocol consisted of the horizontal component of a ground motion record that is repeatedly applied to the shaking table with increasing intensity. Finally, the main results of the experimental test are discussed. The damage patterns, drift ratios and base shear are presented for the ground motion sequence. The results are also discussed through a dynamic capacity curve that shows the attainment of different limit states with increasing ground motion intensity. A set of nonlinear numerical simulations, both static and dynamic, using a 3D FE model of the wall verify the experimental study as they report good agreement with the experimental tests and exhibit stable numerical behaviour.

Keywords Three-leaf masonry walls · Weak lime-mortar joints · Full-scale shake table test · Old masonry buildings

1 Introduction

Three-leaf walls represent a typical solution adopted in the past for masonry buildings in many European regions, especially in those mountainous areas where building materials were extracted from quarries. These masonry walls are made of two external slender stone leaves, often un-connected through the wall thickness, and an inner core made of loose

---

aggregates bound together by poor quality lime mortar (Fig. 1a). The inner core is more flexible and has a lower strength than the external leaves. This implies that unless there are elements that connect the two external leaves, under the horizontal and vertical forces that develop during an earthquake the external leaves are slender and unrestrained, with danger of early failure due to instability.

Past experimental studies report that multi-leaf walls show a weak in-plane strength that is strongly connected to the strength of its weakest component (Silva et al. 2014; Carvalho Bello et al. 2020), usually the mortar (Martínez et al. 2013), and to the presence/absence of transversal connections between the two outer leaves (Vintzileou and Tassios 1995). Past earthquakes, such as the 2009 L'Aquila earthquake in Italy (Brando et al. 2017; Matteis et al. 2009) further showed the intrinsic vulnerability of this masonry type where repeated cyclic deformations can trigger delamination of the outer leaves. The latter implies that the wall may crumble before its maximum mechanical shear/flexural strength is achieved. Augenti and Parisi (2010) report that during the
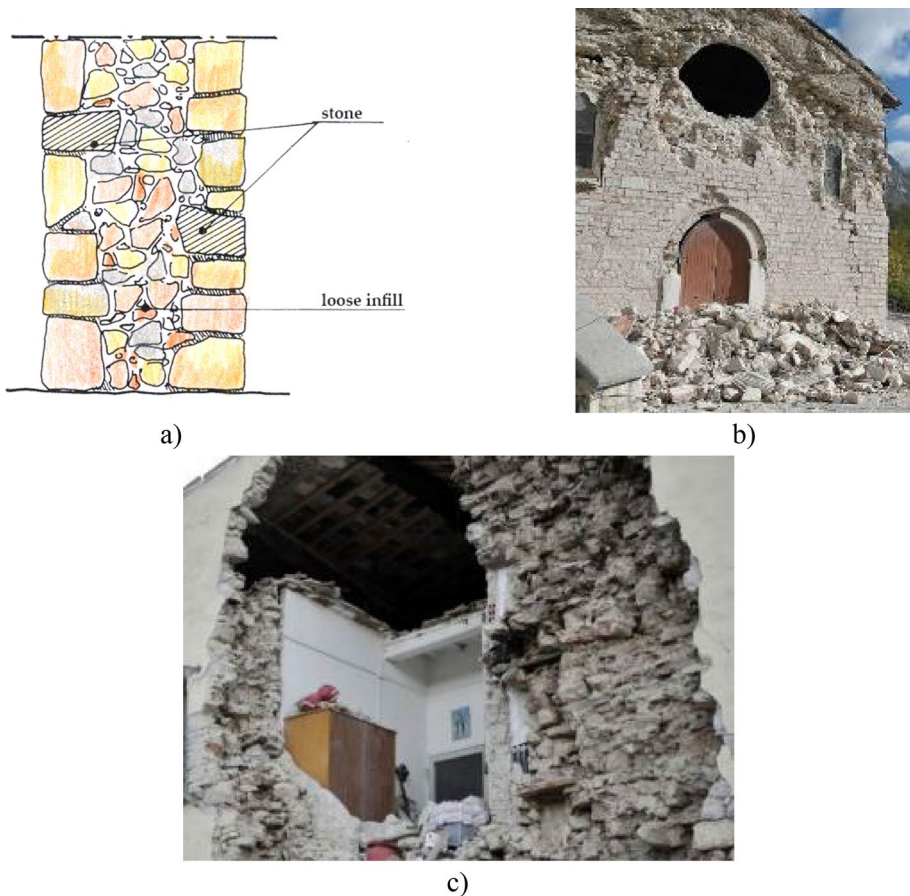

a)

b)

c)

Fig. 1 **a** Example of three-leaf masonry wall cross section; collapse of the three-leaf façade (following the 2016 Central Italy Earthquake) of: **b** the Santa Maria Assunta Church in Ussita and; **c** a residential building in Visso

2009 L'Aquila earthquake 50% of buildings of the historical centres of Onna, Paganica and Castelnuovo, made of multi-leaves masonry walls, completely collapsed.

Similar problems were reported after the more recent 2016 Central Italy Earthquake (Saretta et al. 2016): several façade walls, although often strengthened by steel ties applied at each floor after the 1997 Umbria and Marche earthquake to prevent out-of-plane overturning mechanisms, experienced delamination of the outer leaves (Fig. 1b, c). The intrinsic out-of-plane weakness of three-leaf masonry walls was also documented after the 1998 earthquake in the Azores (Portugal), where several religious buildings were strongly affected by out-of-plane failure (Pereira 1998).

Experimental investigations on the out-of-plane behaviour of multi-leaf masonry walls have been recently carried out (Ramalho et al. 2005; Derakhshan et al. 2013). Among these, it is worth reporting the research presented in Mazzon et al. (2010) and Giaretton et al. (2017) where shaking table tests were performed in order to investigate the effectiveness of different strengthening techniques in enhancing the capacity of the outer leaves of the wall to prevent overturning mechanisms.

It is worth noting that although delamination seems to be the commonly observed pathology of multi-leaf masonry walls, the intrinsic vulnerability of their inner core leads to a weak in–plane behaviour as well, depending on the types of boundary conditions applied on the wall (Binda et al. 2006). For low, mainly elastic states of stress, lateral expansion due to the compression forces on the internal core pushes the outer leaves in the out-of-plane direction. This phenomenon favours the creation of second order effects that, in the absence of a connection mechanism, could lead to the brittle detachment of the external leaves (Oliveira et al. 2012). For higher stresses, if the above delamination does not take place and/or is prevented, the internal core tends to fail and its limited amount of load is transferred to the stiffer external leaves leading to in–plane failure (Pappas 2011). The presence of stone diatones may improve the wall behaviour (Casolo and Milani 2013), as shown in Cascardi et al. (2020) by means of pseudo-static tests on scaled three leaf masonry panels and the empirical model derived for the prediction of the shear strength of the walls.

Another factor that may negatively affect the seismic behavior of three-leaf masonry walls is the change in the vertical force on the wall (Brando et al. 2015; Vintzileou 2011), as a result of the vertical component of the earthquake ground motion which is particularly relevant in near field conditions. This is associated with the repeated cycles of varying vertical load on the masonry walls that may either reduce the compression (Egermann and Neuwald-Burg 1994) and hence diminish their shear strength, as shown by Borri in (2010) or can increase the axial force leading to lateral expansion of the inner core. Notwithstanding the above research findings, the seismic performance of three leaf masonry walls under triaxial earthquake excitation has not yet been fully understood.

Along these lines, this paper presents the main results of a shaking table test that was carried out on a three-leaf wall specimen designed and built compliant to the material properties typically found on sites and traditional construction techniques and details of old masonry buildings met in many Italian historical centres, particularly in Central and South Italy.

The tests presented in this paper are part of a larger test campaign carried out at the EQUALS (Earthquake and Large Structures) laboratory of the University of Bristol as part of the REBOND (Response of as-Built and strengthened three-leaf Masonry walls by Dynamic test) research project, that was funded within the framework of the

H2020-INFRAIA-2016–2017/H2020-INFRAIA-2016–1 SERA (Seismology and Earthquake Engineering Research Alliance) initiative.

The paper is organized as follows: Sect. 2 describes the experimental specimen, its design process and the test setup; Sect. 3 discusses the results obtained from the experimental tests. Section 4 presents a 3D FE model of the specimen and discusses the results of static and dynamic analyses. Finally, Sect. 5 presents the main conclusions that can be drawn from the experimental tests and the relevant numerical simulations.

2 Experimental test set up and specimen design

2.1 Preliminary material tests

Preliminary tests were carried out at the SCAM (Sperimentazione, Controllo, Analisi e Modelli) laboratory of the University "G. d'Annunzio" of Chieti-Pescara, Italy to mechanically characterize the materials of the wall components (Bathe 2007). Preliminary tests were carried out because the wall materials were sourced in Italy—although the tested wall was eventually built at the EQUALS laboratory in Bristol. The main idea of the preliminary tests was to reproduce the geometry, the connections and the material properties typically found in three-leaf masonry wall buildings in Italian historical centres (Roselli et al. 2019) and pave the way for the design of the large scale test by verifying similitude laws from one scale to another.

The stone used was a regular limestone block (calcareous natural stone) typical of Pacentro in the L'Aquila area, Italy. Uniaxial compression tests on ten $70 \times 70 \times 70$ mm stone cubes were carried out according to the Italian standard UNI EN 1926: 2007 (UNI-Ente Italiano di Normazione 1926). The tests provided a mean compressive strength $f_{c,B}$ of 80 MPa. The standard deviation of the compressive strength is 4.5 MPa, corresponding to a coefficient of variation of 5.6%, as reported in Bathe (2007).

To obtain mechanical characteristics similar to those of mortars typically found in three-leaf walls, the composition reported in Table 1 was used. This air lime mortar was designed to have a compressive strength of about 1 MPa. The mortar was mostly lime obtained from crushed limestone and natural aggregates with granulometry between 4 and 16 mm. A superplasticizer admixture was added to reduce the strength to the appropriate level.

Uniaxial compression tests on seventeen $70 \times 70 \times 70$ mm mortar cubes were carried out, according to the UNI EN 1015-11 standard (2019), at different curing times: seven coupons at 7 days, three at 14 days and seven at 28 days. Indeed, at the beginning of the experimental campaign 10 specimens for each curing time were planned to be

Components	% in weight	For 20 kg of mortar
Powdered lime	31.15%	6.23 kg
Natural aggregates (4–16 mm)	68.54%	13.71 kg
Superplasticizer	0.31%	0.06 kg
Water		5 kg
Sum	100%	20 kg + 5 kg of water

Table 1 Mortar composition (Manos 2020)

Fig. 2 Mortar stress–Strain diagrams for uniaxial compression tests at different curing times
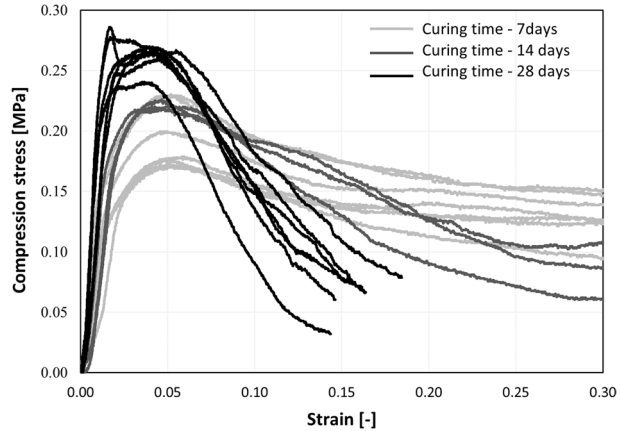
Table 2 Filling material mixture

Component for FM	% in weight	For 120 kg of FM
Mortar	42%	50 kg
Pebbles	58%	70 kg
Sum	100%	120 kg

tested. However, issues related to the consistency of some specimens arose when they were removed from the mould and the number of specimens had to be reduced. Figure 2 shows the resulting stress–strain diagrams. The curing process induced an increase of the compressive stress which returned a mean value $f_{c,M,28}$ around 0.18 MPa at 7 days, 0.24 MPa at 14 days and approximately 0.29 MPa at 28 days. A reduction in the ultimate strain was also observed. The average mortar Young's modulus $E_{c,M}$ was estimated equal to 25 MPa.

No further investigations on the mortar strength were carried out after 28 days, as this is the time conventionally used to measure its strength. On the other hand, the wall was tested at a later stage and the mortar strength at the time of testing was most likely higher. For the filling material (FM), the current literature does not provide precise information about its composition or any specific rule about the mixture to be used. It is clear, however, that the strength of this loose "material" is low, since it is made of waste material held together by very weak mortar. A mix of mortar and pebbles was designed for the proposed test with the mixture details reported in Table 2.

The mortar used for the FM had the same composition as given in Table 1. The FM pebbles' diameters were selected in the 10–80 mm range. Five compression tests were carried out on the FM, showing a mean strength $f_{c,FM} = 0.45$ MPa and a mean elastic modulus $E_{c,FM} = 50$ MPa. It should be mentioned that the sizes of the tested mortar specimens ($70 \times 70 \times 70$ mm) are not consistent with the size indicated by the UNI EN 1015-11 testing protocol but were imposed by the mould sizes available in the laboratory.

2.2 Test wall design

The geometry of the test wall and the vertical gravity loads applied were selected to reproduce the loading conditions on a wall at the top floor of a hypothetical masonry building, which was assumed having height h = 1600 mm and length l = 2000 mm. It was assumed that the wall was topped by a 400 mm high ring beam. The beam was assumed stiff enough to restrain all top rotations, thus fixed–fixed boundary conditions were assumed for the 1600 mm high wall. This design was motivated by three main reasons. First, walls at the top floor often have a lower height due to the presence of pitched roofs. As a result, the shear span is small and may induce shear failure rather than compression/bending failure. *Second*, top floor walls have lower axial loads and this is an advantage given the limited payload of the shaking table. Most importantly, the reduced vertical load with respect to similar walls at the lower floors leads to a lower wall shear strength. To further limit the weight on the table and the size of the wall, a specimen with approximately half the wall height was tested: The specimen top represents the point of counter flexure of the full height wall, thus the boundary conditions are fixed at the base and free at the top. The test specimen had total height h = 1085 mm (790 mm wall plus 295 mm above the timber beam), length l = 2000 mm and total thickness t = 455 mm, that is equal to the sum of the thicknesses of the two outer leaves (t_{out} = 140 mm) and that of the infill core (t_{core} = 175 mm). Three main failure mechanisms were considered for the wall design:

(a)   In-plane shear failure due to diagonal cracking, as expressed by the capacity equation of Turnšek and Čačovič (1971):

$$V_{Rd} = l \cdot t \frac{f_{tb}}{b} \sqrt{1 + \frac{\sigma_0}{f_{tb}}} \tag{1}$$

where $\sigma_0 = N/(l \cdot t)$ is the mean normal stress, N is the axial force applied at the wall centre (assumed positive in compression), $f_{tb} = 1.5 \, \tau_0$ is the masonry tensile strength, where $\tau_0 = 0.043$ MPa is the assumed shear strength value, and b is a corrective coefficient that depends on the section stress distribution and on the wall slenderness ($1 \le b = h/l \le 1.5$). This above value corresponds to a low-quality masonry according to Circolare 21 Gennaio (2019) and was used for the preliminary wall design only.

(b)   Shear failure by sliding, in cases where the shear demand exceeds the shear capacity provided by Eq. (2):

$$V_t = l' \cdot t \cdot \left(\tau_0 + 0.4\sigma_0 \right) \tag{2}$$

where l' is the depth of the cross-section portion that is in compression and τ_0 is the shear stress strength of the masonry with zero axial stress.

(c)   Failure due to compression—bending for a shear force given equal to:

$$V_P = \frac{M_u}{h} \tag{3}$$

where M_u is given by:

$$M_u = \left(l^2 \cdot t \cdot \frac{\sigma_0}{2}\right)\left[1 - \sigma_0/(0.85 \cdot f_{cd})\right] \tag{4}$$

and f_{cd} = MPa is the assumed masonry compressive strength (assumed similarly to τ_0).

The previous equations lead to the strength domain envelope given in Fig. 3 in terms of shear strength vs. axial force. Based on the above calculations and to facilitate the development of shear failure with diagonal cracks, a total vertical load of 66 kN was imposed on the wall top. It is noted that this load, added to the wall weight, was also deemed optimum for the shaking table as it did not exceed the permissible payload, while still allowing accelerations higher than 1 g to be achieved.

2.3 Wall specimen

The wall specimen consisted of three different main components: (*i*) the foundation system; (*ii*) the wall body and; (*iii*) *the* roof supporting additional masses.

2.3.1 Foundation system

The foundation system, schematically shown in Fig. 4, consisted of a reinforced concrete (RC) slab confined at its edges by $254 \times 146 \times 46$ UB steel members. It was designed to support the wall and the additional top mass during the dynamic tests, as well as to withstand the forces and deformations that developed during the construction stages, particularly when the slab was lifted and positioned on the shaking table. The foundation shape was necessary to accommodate additional tests on T-shape walls, that are not discussed in this paper but will be the subject of future publications.

The RC slab was made of a C35/45 concrete and was reinforced, both top and bottom, with A252 steel ($f_y = 460$ N/mm^2) 8 mm-diameter square mesh sheets with a 200 mm on-center. Figure 5 shows selected working phases during construction.
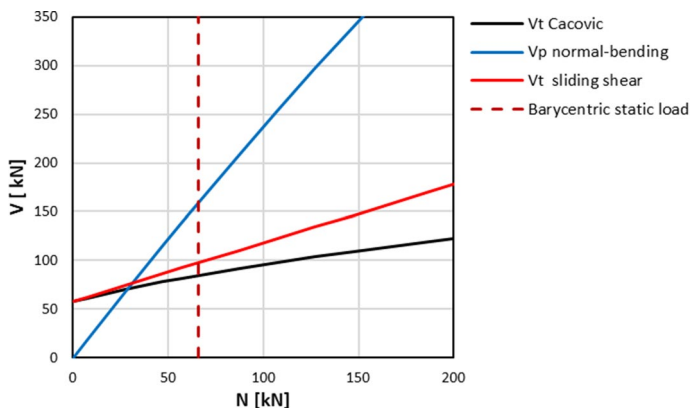

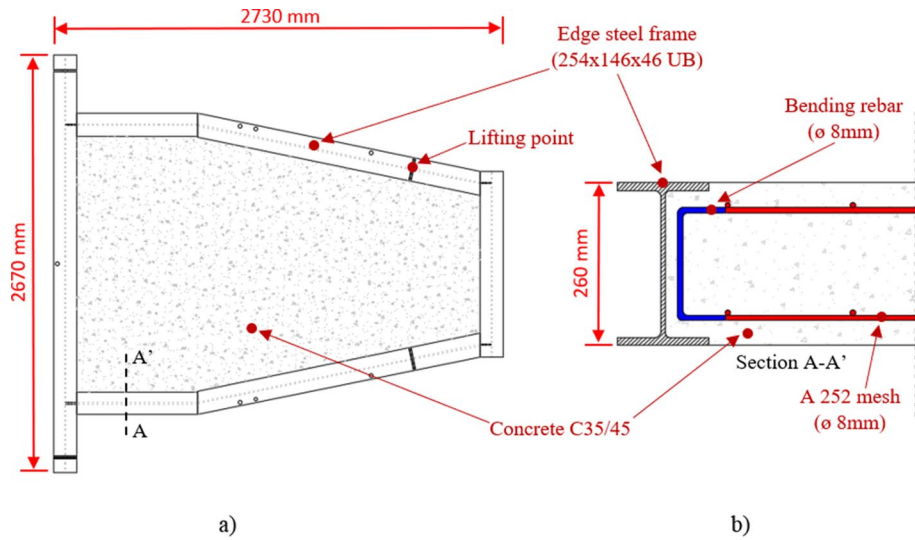**Fig. 3** Strength domain envelope of the test wall specimen

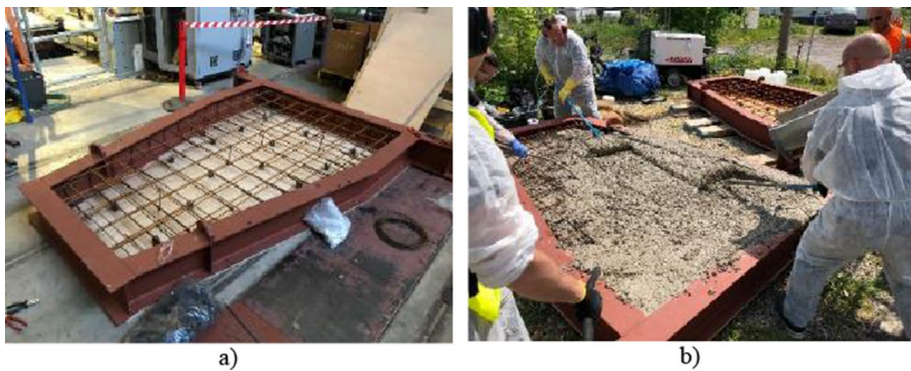**Fig. 4** Specimen foundation system: **a** plan view and **b** section near the foundation edge

Fig. 5 Selected images from construction of the foundation system: **a** edge steel frame with rebar mesh and **b** concrete casting

2.3.2 Masonry wall

Drawings of the tested specimens with the relevant dimensions are shown in Fig. 6. The two outer W and E leaves were made with $350 \times 140 \times 140$ mm blocks, whereas $300 \times 140 \times 190$ mm stones were used transversally to laterally close the wall. The blocks were separated by 15 mm-thick mortar joints in both the vertical and horizontal directions. This joints thickness represents the size one can observe in old buildings (Cocco et al. 2019; Brando et al. 2021). Although the higher end of the range selected for the mortar aggregates (4–16 mm, as mentioned in Sect. 2.1) would not be acceptable today for 15 mm thick mortar joints, they are compatible with the building practice of the past, when modern grinding technologies were not available. Furthermore, 16 mm is the largest size of the aggregate, thus it can still fit in the mortar thickness with the longest side parallel to the
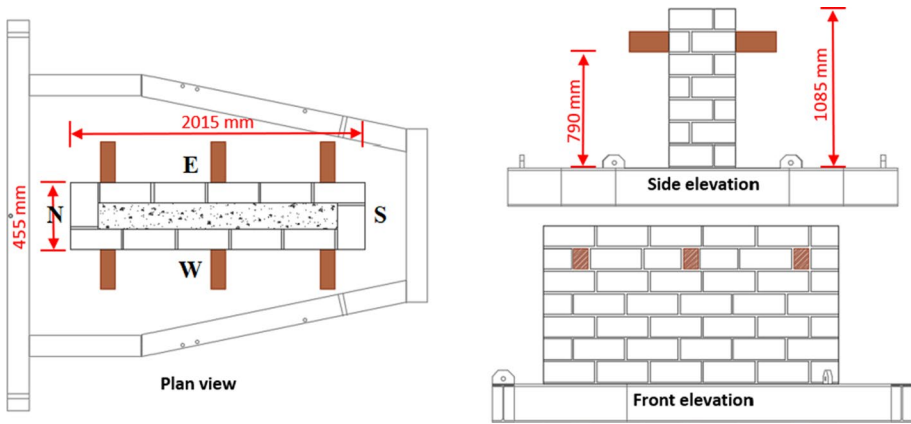
Fig. 6 Wall specimen: plan view, side elevation and end elevation. W (West), E (East), N (North), S (South) in the plan view indicate the four lateral leaves

mortar plane. As previously described, the specimen was completed with an inner infill made of loose materials kept together by poor-quality filling material.

To support the top roof system, three transversal 1000 mm long timber beams were built in the wall top at a height of 790 mm. The timber beams had a 100×140 mm rectangular section and were designed to withstand the shear force transferred by the top weights. Figure 7 depicts relevant working phases of the wall built-up.

2.3.3 Roof supporting additional mass

The roof system consisted of the steel horizontal frame shown in Fig. 8 connected to two longitudinal timber beams that were, in turn, supported by the three transversal timber beams built into the masonry wall. The two longitudinal timber beams were connected to the three transverse timber beams using 12 mm-diameter steel treated rods. The steel frame was made of four longitudinal UB $254 \times 146 \times 43$ profiles connected to two UPE 270 profiles in the orthogonal direction. The total in-plane dimensions of the frame were

Fig. 7 Wall construction phases: **a** infilling between the outer leaves; **b** finished three-leaf wall
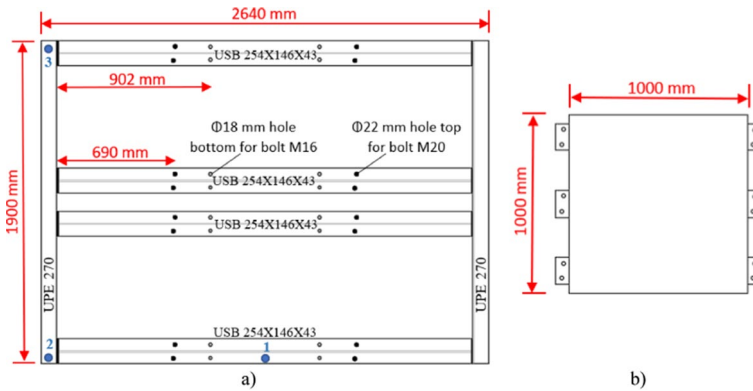
Fig. 8 **a** Horizontal steel frame mounted on top of the wall; **b** 130 mm-thick 1000×1000 mm plate used as additional mass (1-ton weight for a single plate). Numbered and coloured blue dots indicate position of accelerometers shown in Fig. 12

2640×1900 mm. The two 1900 mm-long longitudinal timber beams had a 140×200 mm rectangular cross section. Figure 7 shows relevant working phases of the wall built-up.

On top of the steel frame, six additional masses consisting of 1000×1000×130 mm steel plates (Fig. 8b), each weighing 1 ton, were added. A total mass of 6.5 tons (0.5 tons for the steel frame and 6 tons for the additional steel plates) was added to the top of the wall. This total added mass is the sum of the following contributions: the mass of the half wall on top of the tested wall, the mass of the ring beam on the wall top plus the mass of the tributary area of the roof transferred to the wall top. Figure 9 shows the specimen mounted on the shaking table before testing. To protect the shaking table from damage due to possible overturning of the horizontal frame, two external steel frames were added parallel to the wall. These two protective frames were connected to the shaking table, but interaction with the horizontal steel frame (and thus with the wall) during the test was avoided by creating a 50 mm gap between the top of the frames and the underside of the loading system.

To summarize, construction followed the following sequence. The foundation system (Fig. 5) was built outside the laboratory. Once finished it was transported inside the lab next to the table. The wall specimen was then built on the foundation before lifting foundation and wall specimen onto the shaking table. Once on the table, the lateral support system was added first, followed by the additional top frame and top weights. The total specimen weight was 13.5 tons: 3 tons for the foundation system, 3.3 tons for the wall, 6.5 tons for the roof system, including the additional masses, and 0.7 tons for the two external frames.

2.4 Shaking table

The 6DOF (Degrees Of Freedom) shaking table (i.e., Earthquake Simulator, ES) of the EQUALS Laboratory was used to carry out the dynamic test on the wall. The table is made of a 3 m×3 m cast aluminium platform (Fig. 10a), capable of carrying a maximum payload of 15 tons, but no more than 10 tons at a maximum acceleration of 1.6 g. The platform surface is an arrangement of five superimposed aluminium plates with a regular grid of holes that serve to mount the specimens to the platform through M12 bolts. The platform is supported by eight hydraulic actuators (four horizontal and four vertical, Fig. 10b) that allow all six degrees of freedom to be controlled.

Fig. 9 Wall specimen before the test

2.5 Seismic input

The selection of the seismic input was a key point in the experimental campaign that was conceived to investigate several aspects of the seismic behaviour of three-leaf masonry walls. Following Di Michele et al. (2020), several records were initially considered and the 1976 Gazli earthquake, recorded at the Karakyr station on soil type C, was selected. It is characterized by a moment magnitude (M_w) of 6.8 and a Joyner–Boore (R_{jb}) distance of 3.92 km (Boore and Joyner 1982). The horizontal (one of the two recorded) ground motion record and its corresponding pseudo-acceleration spectrum are represented in Fig. 11. The Peak Ground Acceleration (PGA) is 0.70 g.

The testing sequence started with two preliminary white noise tests carried out with random and low intensity vibrations, respectively. It was originally planned to apply the above ground motion record sequentially with increasing scale factors, more specifically: 10% (PGA = 0.07 g), 25% (0.18 g), 50% (0.35 g), 75% (0.53 g), 100% (0.70 g), 120% (0.84 g), 140% (0.98 g). The scale factors were intended to cause increasing (yet inevitably cumulative) damage levels in the specimen up to collapse. The test with the 100% scaled ground motion was repeated twice because the first run caused major damage (discussed in detail in §3.2) and it was thought that a second run with the same intensity might induce collapse. Since this did not actually happen, it was decided to continue the testing with a ground motion scale factor of 140%, thus skipping the 120% run. In retrospect, the 120% run would have given useful additional information on the damage evolution given that the specimen went from severe damage for the 100% run to total collapse in the 140% run. Table 3 summarizes the testing sequence.
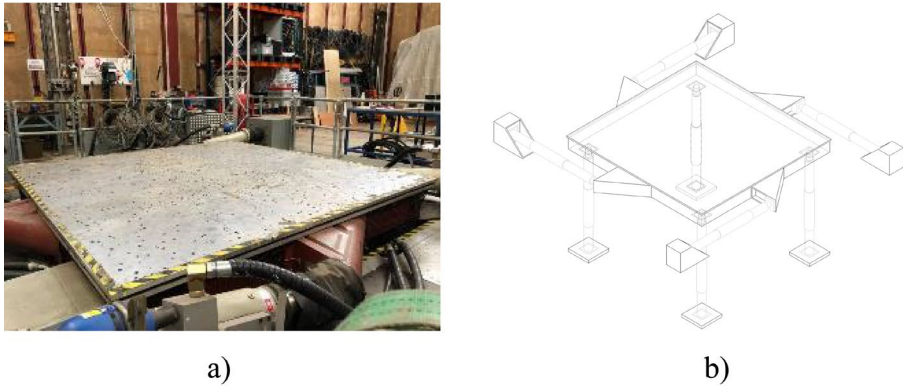
Fig. 10 The shaking table of the EQUALS laboratory at the University of Bristol

2.6 Data acquisition system

The data acquisition system consisted of a combination of Infrared Vision instrumentation together with high speed video (HSV) (Dihoru et al. 2019) for tracking, in real time, the position of reflective markers mounted on the specimen (Fig. 12a). This system worked in parallel with the accelerometer data collected by a conventional data acquisition (DAQ) system.

Displacements in the three directions (X, Y and Z) were recorded with five infrared Oqus400 cameras as shown in Fig. 12b. Accelerations were recorded using nine accelerometers around the specimen (Fig. 12c). Three of the accelerometers were arranged on the shaking table to measure the acceleration imposed on the wall and six on the top horizontal steel frame, as shown in Fig. 12c, d. The accelerometers work in a range of ± 10 g with a sensitivity of the order of 10^{-14} g. Acceleration data was recorded at intervals of 2×10^{-4} s.
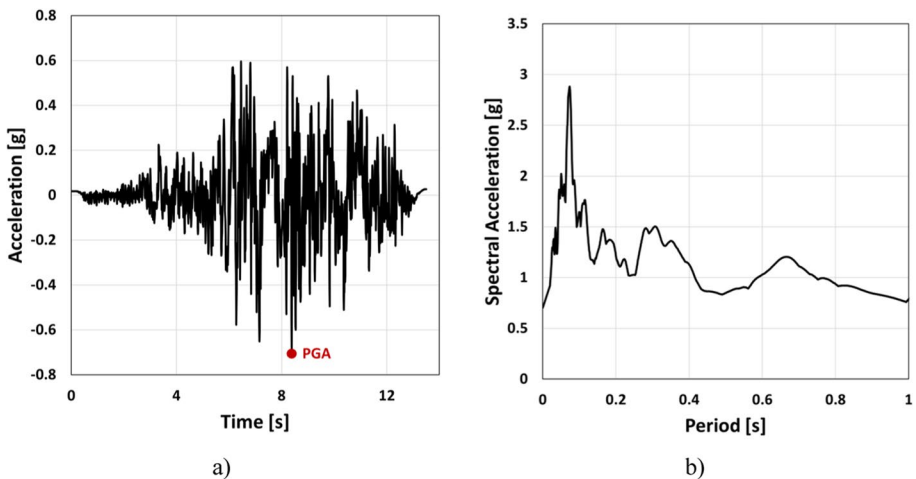
Fig. 11 May 17, 1976 Gazli earthquake: **a** recorded Horizontal (H) component and; **b** corresponding elastic pseudo-acceleration spectrum (for 5% damping)

Table 3 Shaking table test sequence

Test Label	Seismic Intensity	Nominal PGA [g]	Actual PGA [g]	Nominal Sa (T_1) [g]	Actual Sa (T_1) [g]
A1,1	White Noise	–	–	–	–
A1,2	White Noise	–	–	–	–
A2	10%	0.07	0.08	0.14	0.09
A3	25%	0.18	0.20	0.35	0.26
A4	50%	0.35	0.39	0.69	0.46
A6	75%	0.53	0.60	1.04	0.70
A8	1° input al 100%	0.70	0.80	1.38	0.82
A10	2° input al 100%	0.70	0.82	1.38	0.80
A14	140%	0.98	1.11	1.94	1.32
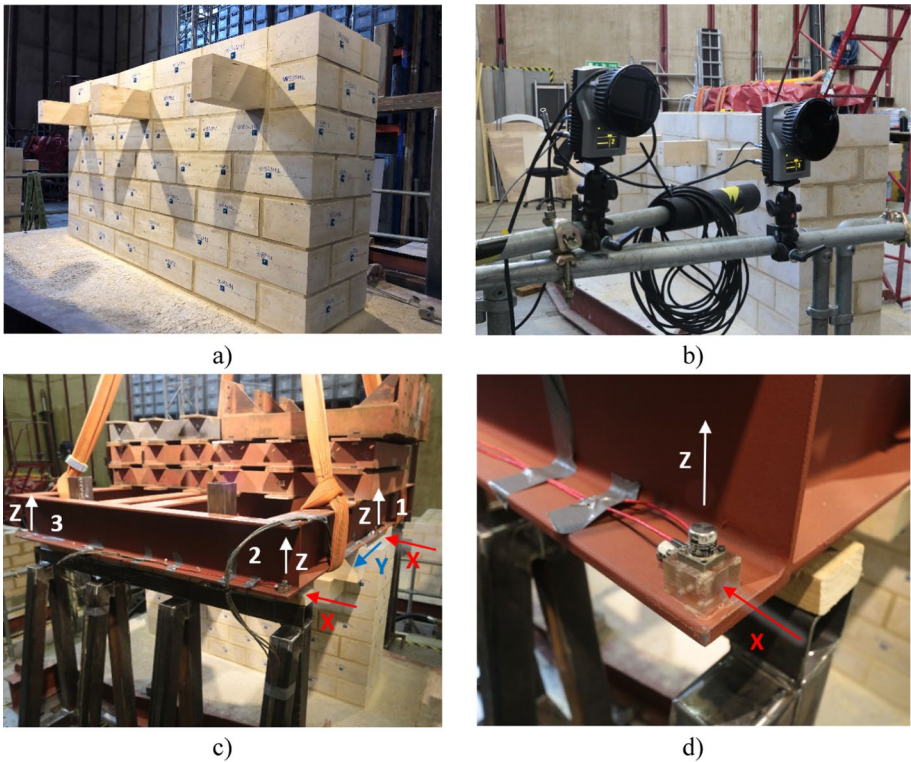
Fig. 12 Main features of the data acquisition system: **a** markers on the masonry faces for displacement measurements; **b** infrared cameras; **c** accelerometers on the top steel frame; **d** close-up of accelerometer 2 on the top steel frame

The data acquisition system allowed monitoring of the following two response parameters, mainly, (a) Drift Ratio (θ) and (b) Base Shear Coefficient (BSC).

3 Test results

3.1 General

First of all, for each ground motion intensity level, the imposed nominal signal was compare with the actual one recorded on the shaking table by the three table accelerometers. Figure 13 compares the two signals in terms of 5%-damped elastic pseudo-acceleration response spectra. Although a good agreement can be observed for periods higher than 0.25 s, some discrepancies in terms of spectral ordinates are evident for high frequencies. This was probably a limitation of the tuning process of the shake table. Similar discrepancies were observed in many other shake table tests around the world, even with tight
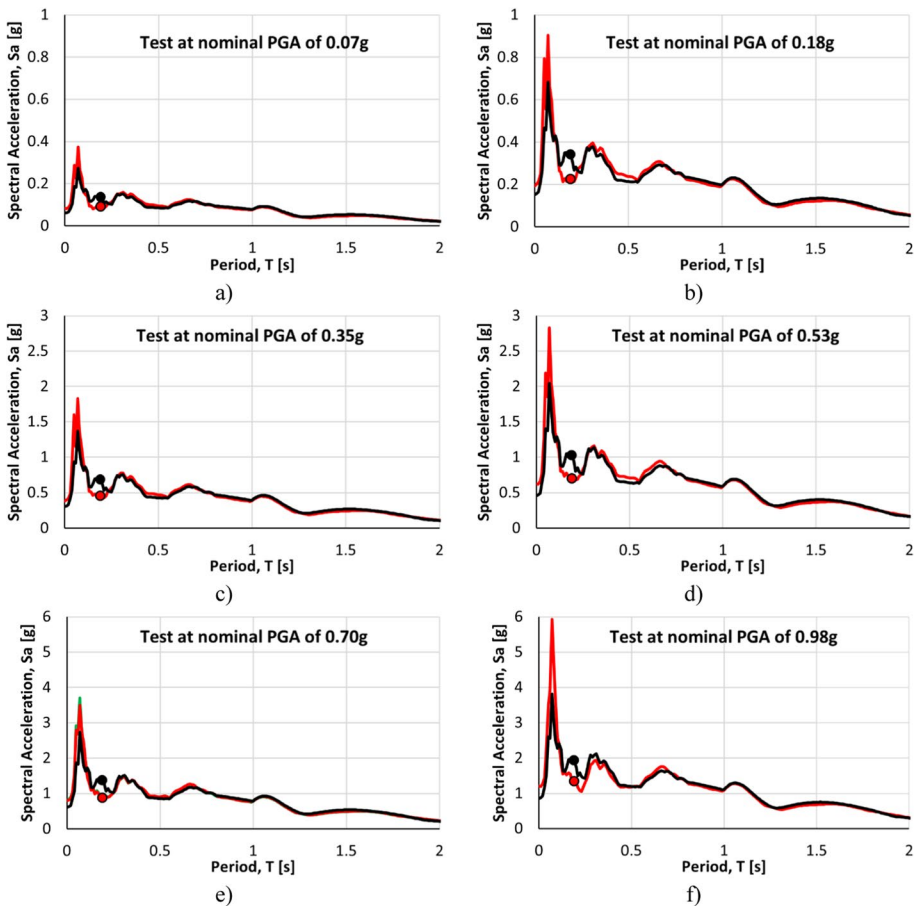
Fig. 13 Comparison between elastic acceleration response spectra (for 5% damping) of the input nominal records (black) and of the records measured on the shaking table (red)

shake-table tuning, such as the USCD-NEES shake table (Luco et al. 2010; Moaveni et al. 2013; Mugabo et al. 2021), and at the Eucentre shaking table facility in Pavia, Italy (Magenes et al. 2014).

The maximum accelerations recorded on the shaking table (corresponding to zero natural period in Fig. 13) were, on average, 13% higher than those of the input signals. The spectral acceleration values near the initial fundamental period in the specimen longitudinal direction (which the white noise tests identified as $T_1 = 0.18$ s) calculated from the shaking table signals were always lower than those of the input signals (see the black and red bullets in Fig. 13), with a maximum difference of 32%. It should be pointed out that when damage occurs for higher ground/spectral accelerations, the period of the structure increases significantly, and this should lead to the conclusion that the actual and the nominal ground/spectral accelerations tend to diverge for higher shaking intensities.

Table 3 summarizes the seismic sequence applied to the specimen. Each imposed ground motion is labelled in the first column and is defined in terms of input seismic intensity, nominal and actual PGA, nominal and actual spectral accelerations S_a at the fundamental period of the specimen $T_1 = 0.18$ s.

3.2 Observed damage and failure

The evolution of the wall damage for increasing accelerations was carefully monitored during the tests. The specimen developed minor cracks during lifting and transportation onto the shaking table due to the low strength of the weak mortar and possibly to the difference in stiffness between the external leaves and the more flexible inner core. Following a check of these cracks, they were not considered of structural significance. Additional small cracks due to shrinkage appeared near the timber beams (Fig. 14), where the timber locally absorbed water from the mortar, thus affecting its curing. These small cracks may have affected the response of the specimen in the first runs with low accelerations by slightly reducing the wall initial stiffness.

The specimen did not show any remarkable damage before test A6 [nominal PGA = 0.53 g], when small—mostly vertical—cracks were detected at the mortar joints, more specifically below the external timber beams (Fig. 15). These in plane cracks on the two external W and E leaves slightly widened during test A8.

At the end of test A10, corresponding to a nominal PGA = 0.70 *g,* delamination of the two outer N and S leaves started, with important vertical cracks developing (Fig. 16b). Moreover, narrow in-plane shear cracks appeared on the two W and E leaves (Fig. 16a). An incipient

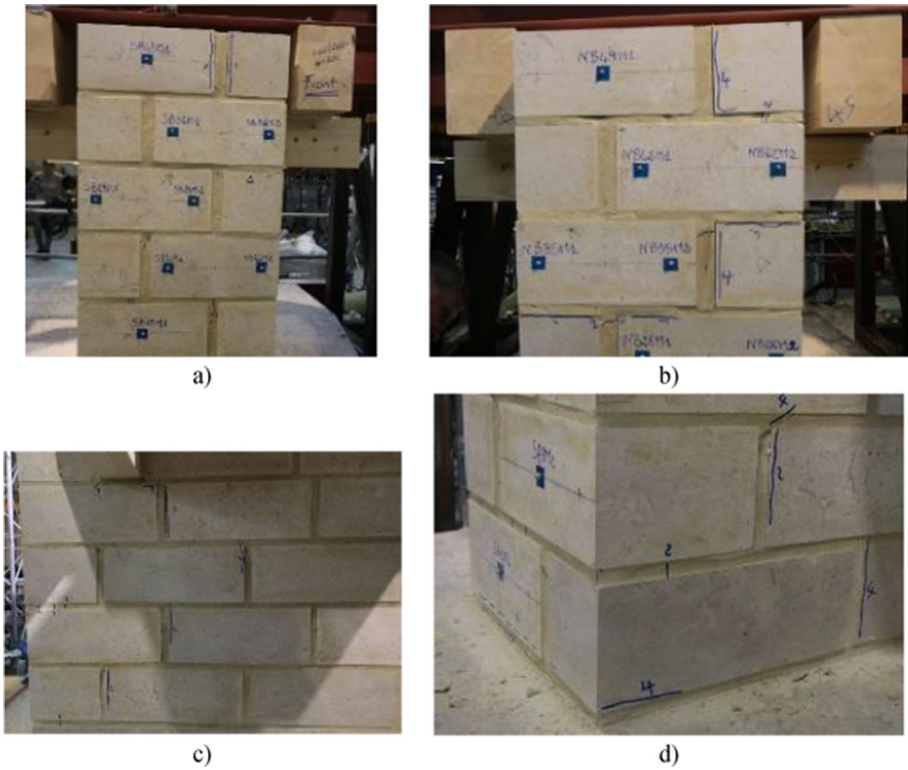**Fig. 14** Mortar cracks due to shrinkage near a timber beam

Fig. 15 Damage at the end of test A6 (nominal PGA=0.53 g) on: **a**, **b** S and N leaves; **c** E leaf; **d** SE corner. Major cracks are marked and numbered in blue
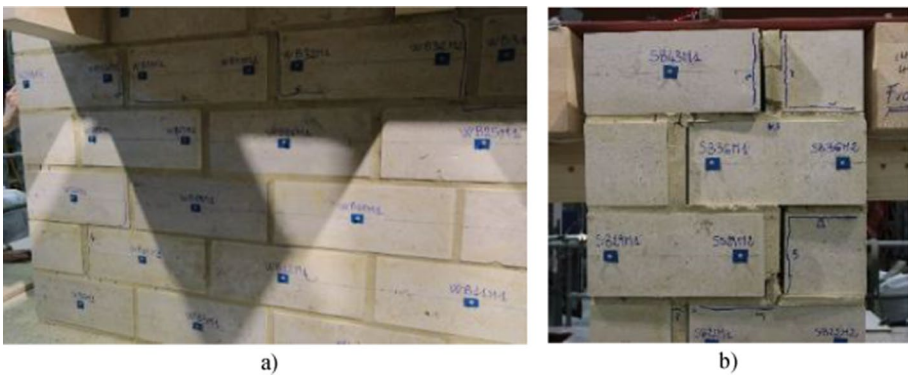

Fig. 16 Damage at the end of test A10 (nominal PGA=0.70 g) on: **a** W leaf; **b** S leaf. Major cracks are marked and numbered in blue
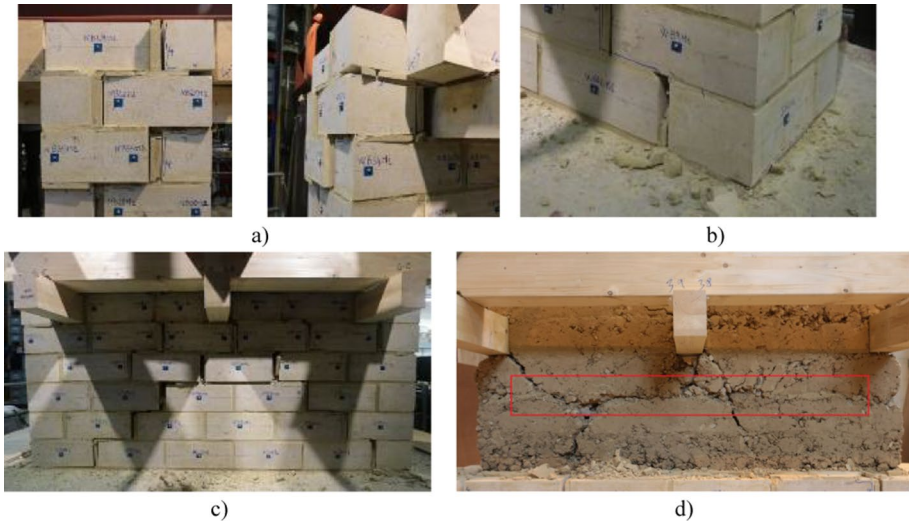
Fig. 17 Damage at the end of test A14 (nominal PGA = 0.98 g): **a** at the wall top; **b** at one of the lower corners; **c** on one of the two lateral sides; **d** in the infill following removal of the stone units of one of the outer layers (the longitudinal, out-of-plane plastic hinge crack is schematically shown inside the red box)

out-of-plane flexural mechanism of the outer leaves was also evidenced by the slight dislocation of the longitudinal blocks in the direction perpendicular to the wall (Fig. 16b).

At the end of test A14 (nominal PGA of 0.98 g), damage was visible throughout the wall, with different mechanisms activated. On the wall two lateral sides, detachment of the two N and S leaves was evident (Fig. 17a). Sliding damage also took place in the lower end corner (Fig. 17b). Diagonal shear cracks (30–40 mm wide) were clearly visible (Fig. 17c). The out-of-plane flexural mechanism of the outer leaves was observed. This mechanism became more evident when the blocks below the timber crossbeams were removed (Fig. 17d). The infill had horizontal cracks pointing to the formation of a horizontal cylindrical plastic hinge. The outer leaf was, however, constrained by the timber beams at the top and by the foundation at the bottom. The leaf basically had two cylindrical hinges parallel to the wall lateral side, one at the top and one at the bottom. The out-of-plane displacements of the outer leaves indicate that a thrusting force in the out-of-plane direction pushed the leaves outward. The poor quality of the infill and the lack of through connections between the two external leaves (typical of poor quality three-leaf walls) are the major causes for the delamination and the undesired out-of-plane bulging of the outer leaves that result laterally unrestrained.

Since the seismic excitation was in-plane, the thrusting force was most likely due to the lateral expansion by Poisson effect related to the increase in the vertical stresses due to the cyclic bending moments on the wall. It is worth mentioning that even for higher accelerations no stone cracked, thus confirming that the mortar represents the weak component of this masonry wall. Finally, no noticeable torsional movements were measured.

Fig. 18 Frequency Response Function (FRF) of the accelerations measured in **a** X, **b** Y, **c** Z directions at the wall top during white noise A1 test

a)

b)

c)
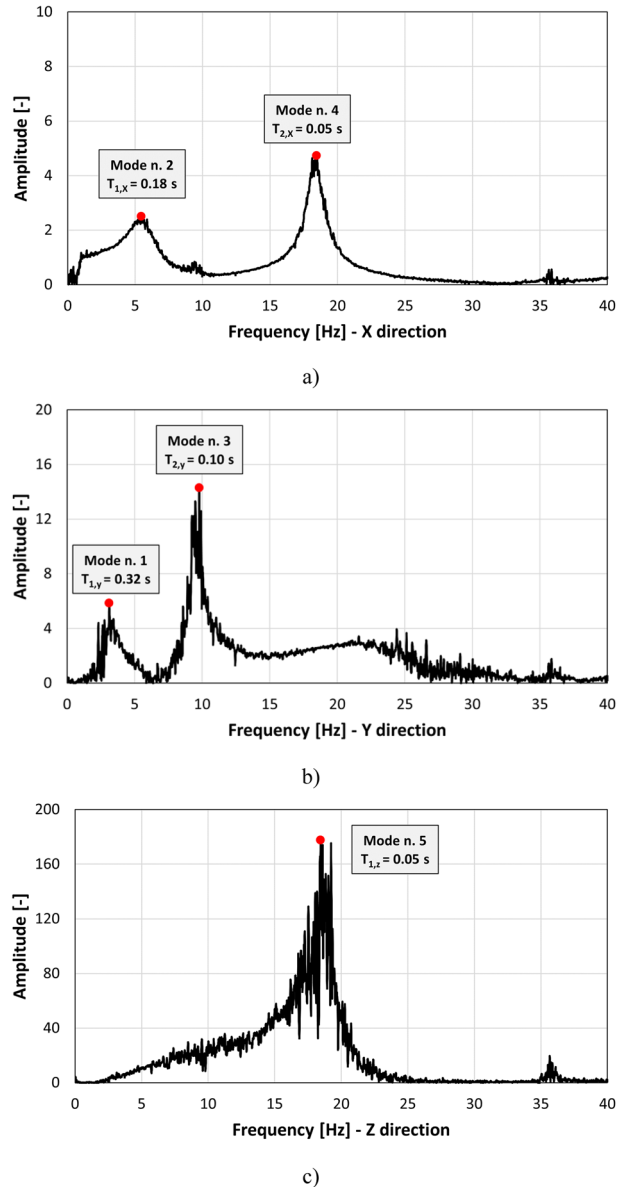
3.3 Results from data processing

3.3.1 Modal identification of wall dynamic properties

Figure 18 shows the Frequency Response Functions (FRFs) of the accelerations measured at the wall top (by accelerometer 1 in Fig. 12c) during the white noise test A1. The graphs show the different peaks (identified by the red dots) that correspond to the main frequencies in the three directions. The first five measured periods are shown in Fig. 18.

The fundamental period T1 in the X (longitudinal) direction, corresponding to the overall second mode, is 0.183 s. Modes 4 and 5 are indicated separately even though they have the same periods. It was not possible to determine whether they are a single mode with components in both the X and Z directions or are two separate modes with very similar frequencies.

3.3.2 Horizontal and vertical displacements

Figure 19 shows the drift ratios $\theta(t)$ measured during the tests from A3 to A14. The drift ratios for test A2 are negligible and are not reported. The drifts were computed from the measured displacements in the X (longitudinal) direction according to Eq. (5), where $\delta(t)_{Top}$ is the average wall top displacement immediately below the central beam (markers from WB30 to WB34 in Fig. 20), $\delta(t)_{Base}$ is the shaking table measured displacement, $h' = 800$ mm is the distance between the two points of measure.

$$\theta(t) = \frac{\delta(t)_{Top} - \delta(T)_{Base}}{h'} \cdot 100 \quad [\%] \tag{5}$$

The results show that significant damage was triggered by the A14 test (140%) with maximum and residual drifts of about 3.24% and 0.30%, respectively. Figure 20 shows the maximum horizontal displacement profiles (including their direction) measured for the two seismic events A10 (100%—blue line) and A14 (140%—red line).
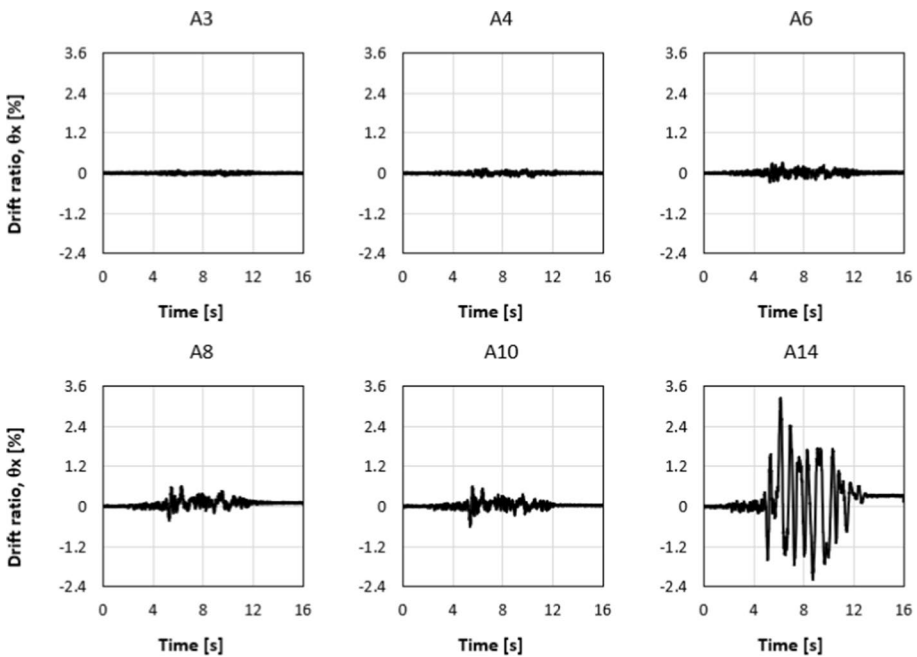
Fig. 19 Measured wall story drift ratios for increasing ground motion intensities. Note that only test A14 resulted into a residual drift of 0.30%
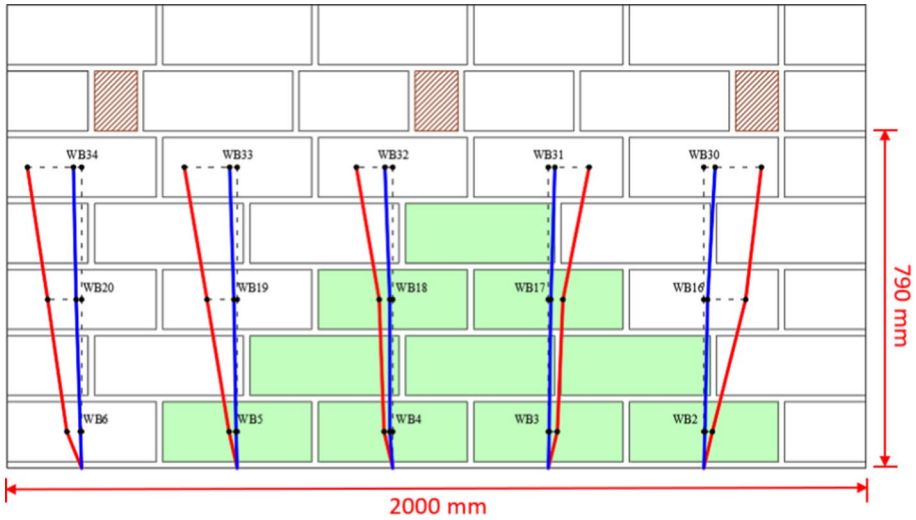
Fig. 20 Maximum horizontal displacements recorded during tests A10 (blue line) and A14 (red line). Displacements are scaled by a factor of 3
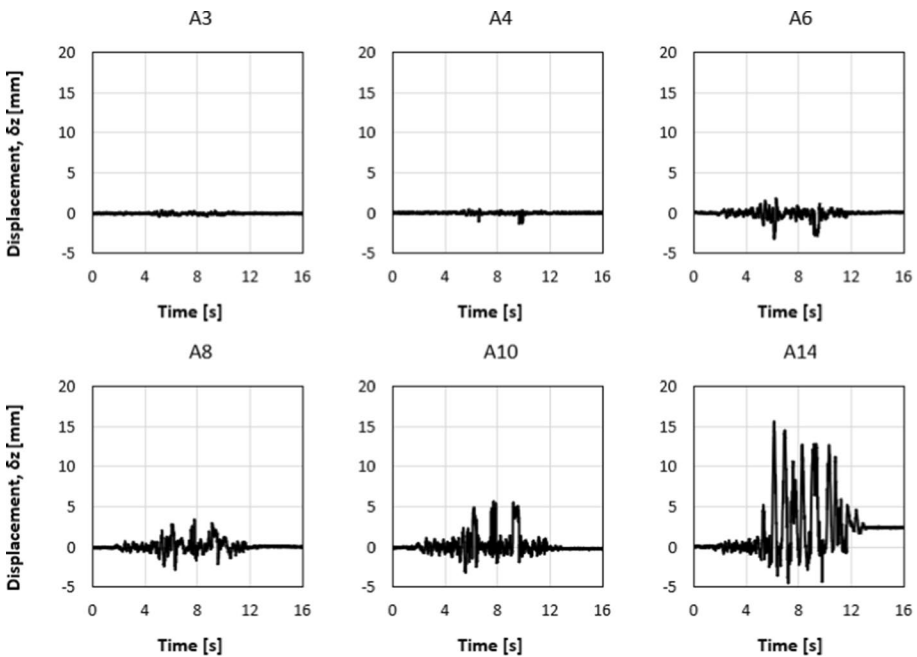

Fig. 21 Vertical displacements for the tested wall under different ground accelerations

There are significant maximum displacement increases between the two tests. The green blocks below the two shear cracks showed little displacement, even during the A14 test. This is in line with the diagonal shear crack pattern clearly visible in Fig. 17c at the end

of test A14. The two diagonal shear cracks limit the forces applied to and, therefore, the displacement of the lower green blocks. The white blocks above the two diagonal cracks tilted and slid along the cracks with displacements significantly larger than those of the green blocks.

Figure 21 shows the vertical displacements δ_z measured during the test at the wall top computed as the average of the displacements of the markers below the cross beams (markers from WB30 to WB34 in Fig. 20). When damage becomes significant, the vertical displacements significantly increase, and this is probably due to the tilting mechanisms activated above the shear diagonal cracks.

The maximum vertical displacements and their directions for tests A10 and A14 are reported in Fig. 22. The rotations α of each block read during tests A10 and A14 are shown in Fig. 23a, b, respectively. These rotations were computed according to Eq. (6):

$$\alpha = \arcsin\left(\frac{\Delta h}{l}\right) \tag{6}$$

where Δh is the relative vertical displacements between the two markers on each block and $l = 270$ mm is the horizontal distance between them (see Fig. 23). The maximum rotation during test A14 was approximately 0.06°, with a residual rotation of approximately 0.02°.

3.3.3 Limit states

The above results can be interpreted with respect to the damage limit states (DL) defined by the Italian CNR-DT 212-2013 Code (2014). In this document the following damage limit states are defined:

- DL3 is the limit condition where no damage is visible. It corresponds to drift values from 0.25 to 0.4% for shear failure and from 0.4 to 0.8% for bending failure;
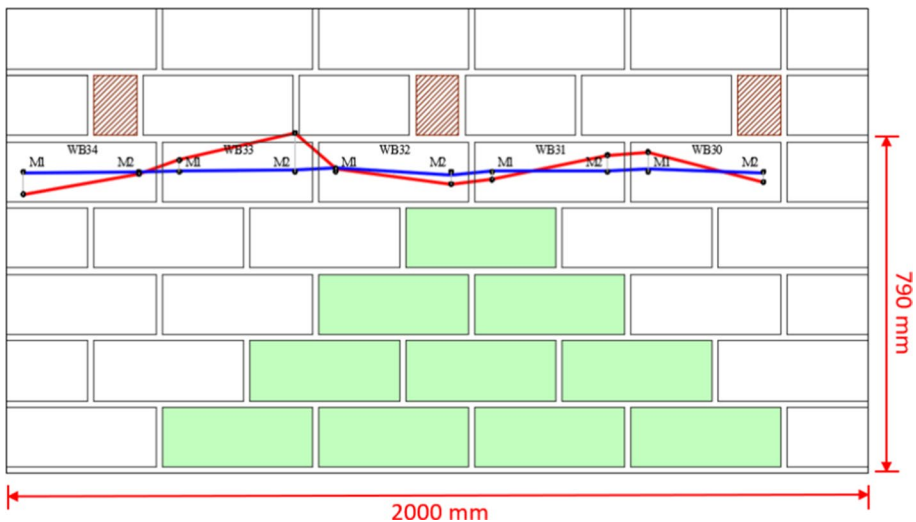

Fig. 22 Maximum vertical displacements recorded on the top of the wall for test A10 (blue line) and A14 (red line). Displacements are scaled by a factor of 10
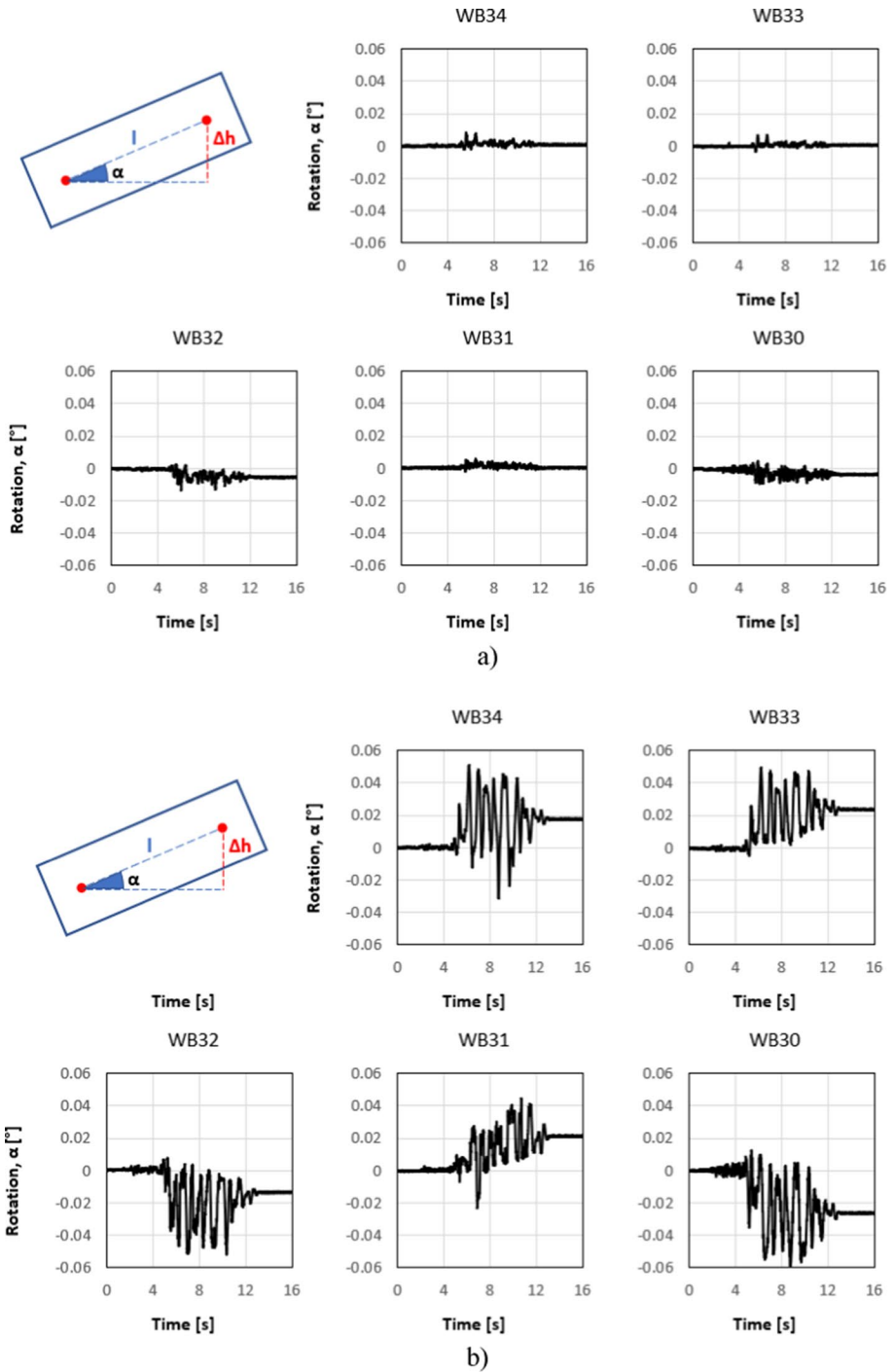
Fig. 23 Rotations of blocks at the wall top during tests **a** A10 and **b** A14

Table 4 Summary of damage limit states reached in the last four tests of the test sequence

Test	Observed Damage	Peak Drift Ratio [-]
A6 – 75% (PGAx=0.53g)		0.30
DL3		
A8 – 100% (PGAx=0.70g)		0.58
A10 – 100% (PGAx=0.70g)		0.60
DL4		
A14 – 140% (PGAx=0.98g)		3.24
FAILURE		

- DL4 is the limit condition where heavy damage is observed. It corresponds to drift values from 0.4 to 0.6% for shear failure and from 0.8 to 1.2% for bending failure;
- DL5 is the limit condition that indicates collapse. It corresponds to drift values from 0.6 to 0.9% for shear failure and from 1.2 to 1.8% for bending failure.

According to the observed failure mode (shear) and to the drifts recorded during the test sequence, it is possible to state that, as reported in Table 4, DL3 was attained in test A6 with a maximum 0.30% drift. Test A8 reached a maximum drift of 0.58%, while test A10 (with the same input ground motion) showed only minor crack increases and a maximum drift of 0.60% corresponding to the upper limit of DL4. Table 4 shows the cracks that formed during the test sequence. The cracks are identified by the red marks, and the increasing thickness indicates larger openings.

Because of the strong intensity increase from test A10 (100% of record) to test A14 (140%), DL5 was bypassed, and the specimen completed failed during test A14 with a maximum drift of 3.24%. It should be observed that another major difference between tests A10 and A14 can be seen in Figs. 19, 21 and 23. Very small residual displacements can be observed at the end of test A10 while significant residual displacements were measured after test A14, thus indicating failure during test A14.

3.3.4 Measured accelerations

Two accelerometers mounted on the top steel frame (one in position 1, the other in position 2, as shown in Fig. 13c) recorded the acceleration responses of the wall in the X longitudinal direction. The measures recorded were very similar for the two accelerometers indicating that that rotation of the specimen and of the roof systems around a vertical axis were negligible. Although the accelerometers were positioned on the top steel frame, it is assumed that the recorded accelerations were equal to those at the specimen top because of the quasi-rigid connection between the roof system and the wall top.

The recorded accelerations in the X direction are reported in black in Fig. 24. The same figure shows in grey the accelerations of the shaking table. The results of test A2 are not shown because the differences between the two signals are not discernible given their very small magnitudes.

The acceleration histories read on the wall top show some unexpected peaks, particularly after test A6, when the first cracks were observed. These peaks increased in the later tests at higher intensities when damage gradually increased. Looking closely at the results from test A14 (though the same trend is observed for the other sequences) the peaks are mostly related to high amplifications at frequencies in the 70–100 Hz range.

This becomes even clearer when comparing the acceleration history at the wall top before and after applying a Savitzky–Golay finite impulse response (FIR) filter (Schafer 2011) that smooths the original signal with a polynomial order equal to 3 in order to mitigate the above frequency effects (see Fig. 25).
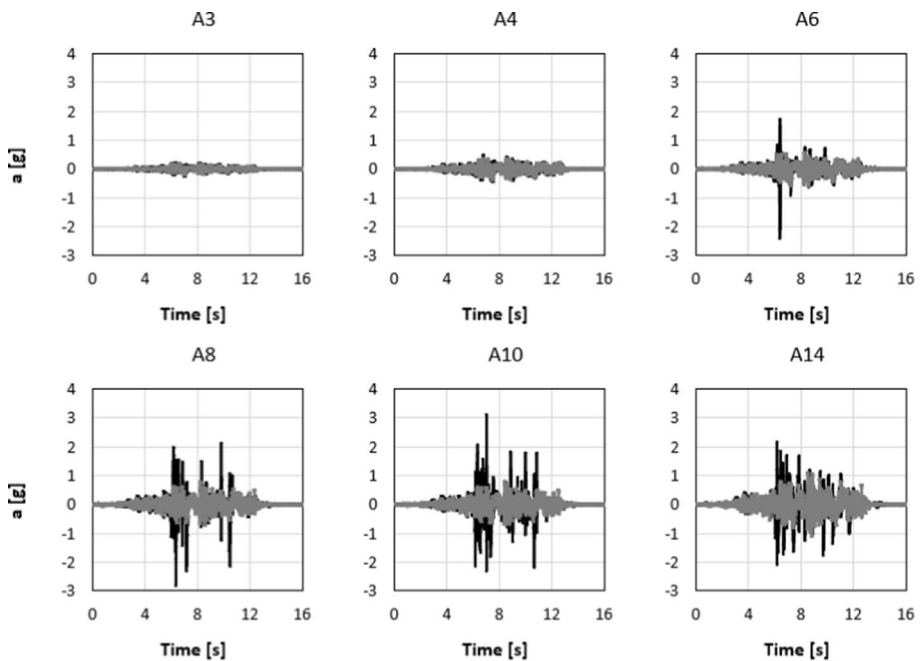

Fig. 24 Acceleration responses in the X (longitudinal) direction for the test sequence from A3 to A14. The accelerations recorded on the shaking table are reported in grey, those recorded at the wall top are shown in black
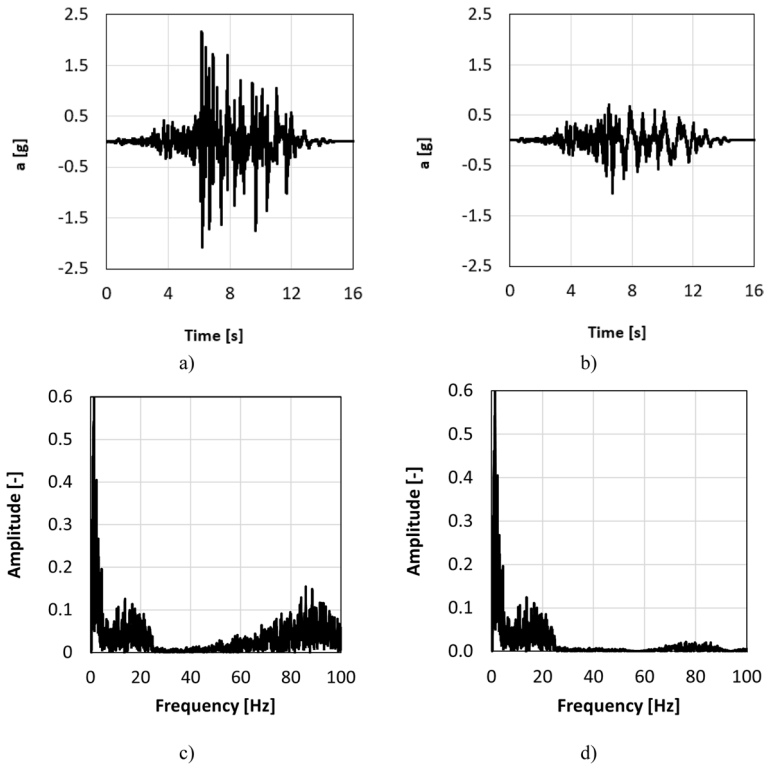
Fig. 25 Acceleration signal at the wall top for test A14: **a** without and **b** with the FIR filter. **c** shows the Fourier transform of signal (**a**) while **d** shows the Fourier transform of signal (**b**)

Figure 26 reports the same data shown in Fig. 24 after applying the FIR filter on the signals recorded at the wall top. The accelerations at the wall top and on the shaking table are now quite similar and this is consistent with the spectra reported in Fig. 13 where the spectral accelerations at and near the wall fundamental period in the longitudinal direction (0.183 s) are similar to the PGA.

Figure 27 shows the cyclic response of the wall top in the longitudinal X direction in terms of filtered accelerations vs. top displacement. The responses obtained for the different tests are plotted in different colours. It is observed that during test A10 (red line), the displacements reach almost 5 mm while the maximum strength is lower than that of test A8, thus indicating that the specimen is near failure since its strength is decreasing. Results for test A14 are not reported in Fig. 27 since they are out-of-scale with respect to the previous tests, further indicating that complete collapse was reached in test A14.

3.3.5 Force–displacement response

The specimen force–displacement response is represented by the maximum base shear coefficient (BSC) vs. drift (or displacement) plot in Fig. 28. The maximum BSC, i.e. the maximum base shear V_B normalized with respect to the total weight, is:
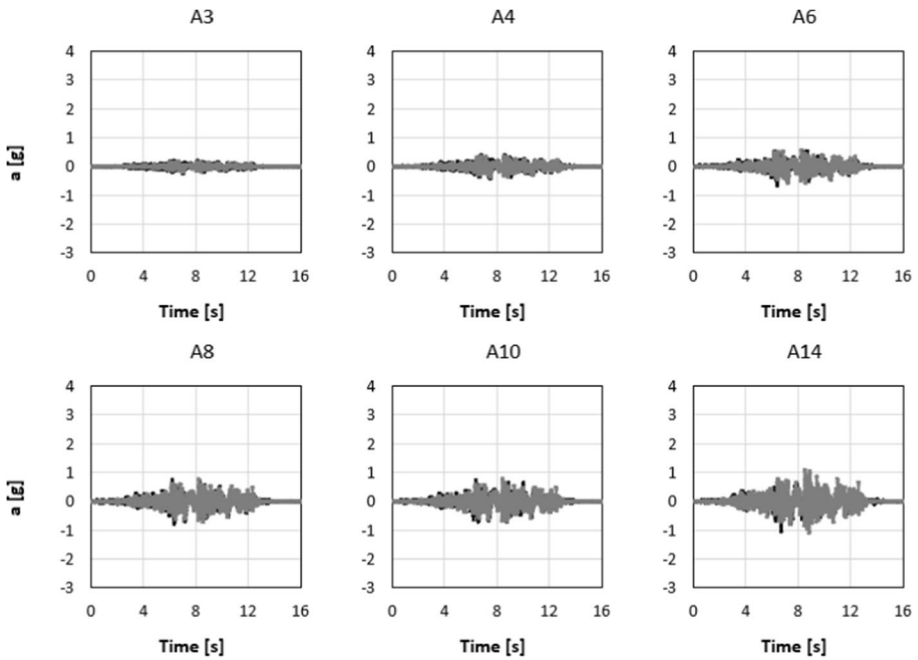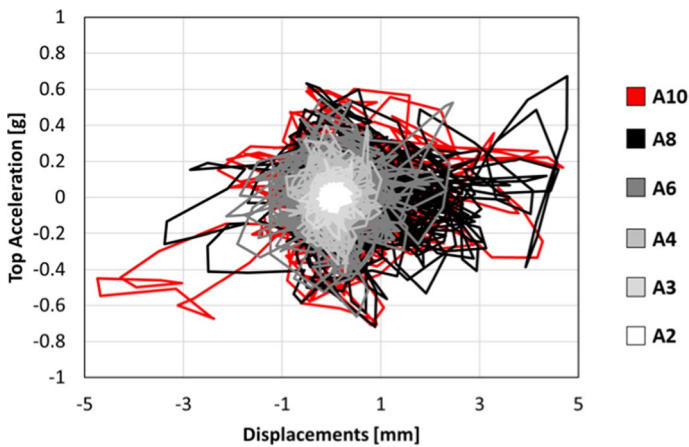
Fig. 26 Filtered acceleration responses in the X (longitudinal) direction for the test sequence from A3 to A14. The accelerations recorded on the shaking table are reported in grey, those recorded at the wall top are shown in black

Fig. 27 Filtered acceleration versus lateral displacement at the wall top

$$BSC = \frac{V_B}{g \cdot m_{TOT}} \tag{7}$$

V_B is computed as the maximum acceleration recorded at the wall top multiplied by the wall seismic mass (m_{TOT}). m_{TOT} is 8.15 tons estimated as half of the wall mass (1.65

Fig. 28 Maximum base shear versus maximum drift ratio for test sequence A2 to A14. Vertical coloured lines indicate upper values of drift ratios corresponding to damage limit states DL3, DL4 and DL5 defined by CNR-DT 212 (2013) for shear critical walls
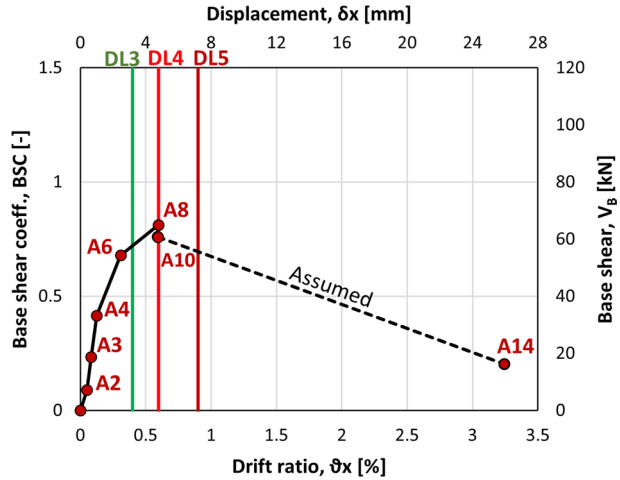
Table 5 Maximum shear (VB) and base shear coefficient (BSC) for each test

Test Name	Nominal PGAx [g]	VB [kN]	BSC [–]
A2	0.07	7.22	0.09
A3	0.18	18.79	0.24
A4	0.35	33.28	0.42
A6	0.53	54.30	0.68
A8	0.70	64.88	0.81
A10	0.70	60.77	0.76
A14	0.98	84.40	1.06

tons) plus the additional top masses (6.5 tons). Half of the wall mass corresponds the mass of the tributary volume assigned to the wall top.

Table 5 reports the shear forces and the corresponding BSC values for the sequence of tests carried out on the wall. The experimental results show that diagonal shear failure was reached for a shear force between 60 and 80 kN, in line with the prediction of the wall capacity (Fig. 3). These BSC values are plotted in Fig. 28 as a function of the corresponding maximum displacements to obtain a capacity curve. The last point of the capacity curve of Fig. 28 has no physical meaning in terms of shear capacity because, as previously observed, after test A10 (penultimate dot of the curve), severe damage with large shear cracks was observed thus the accelerations measured during test A14 on the wall top are mainly due to local mechanisms activated aside the cracks.

The reduced shear strength of point A14 is indicative (it corresponds to the residual strength of 25% the maximum shear capacity as given by the technical document CNR-DT 212, 2013) and simply suggests that the specimen has reached complete failure. Figure 28 also shows coloured vertical lines corresponding to the drift ratio values of the damage limit states introduced in § 3.3.3 and provided by CNR-DT 212, 2013.

The results are those already shown in Table 4. Test A6 is within the DL3 drift range, tests A8 and A10 are at the upper limit of DL4, while A14 is represented by a drift way beyond DL5, confirming full failure. A point within the DL5 range is missing because
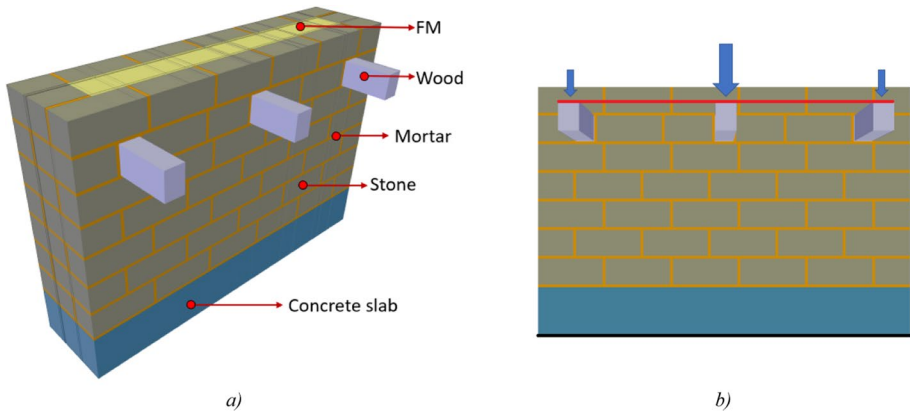
Fig. 29 a Micro-model with brick elements identification; **b** front view of the micro-model with vertical static loads applied on the top of cross-timber beams, Beam Solid Coupling constraint (red line) and fix constraint (black line)

Table 6 Properties of stone, mortar and filling material: self weight, Young's modulus E, tensile strength and fracture energy ft and Gt, compression strength and fracture energy fc and Gc

Material	γ [kN/m³]	E [MPa]	ft [MPa]	Gt [N/mm]	fc [MPa]	Gc [N/mm]
Stone	25.5	20,200	2	0.08	80	450
Mortar joints	16.5	25	0.03	0.016	0.3	80
FM	20.0	50	0.1	0.05	30	60
Wood	10.0	15,000	*Elastic material			
Concrete	25.0	20,000	*Elastic material			

the tests jumped from a scale factor of 100% (A8 and A10) to a value of 140% (test A14).

Additional information on the experimental campaign at hand is available in a digital report in Reference (Di Michele et al. 2021).

4 Numerical analyses on three-leaf masonry wall

4.1 Introduction and model definition

The experimental tests presented in the previous sections were complemented by numerical simulations whose aim was to validate the experimental results, complement them in case of missing measurements and verify the effectiveness of available modelling techniques in terms of mechanical performance and numerical stability. The wall specimen was modelled using a continuous micro-model with brick elements (bbarBrick) for the different materials that make up the wall (Fig. 29a). STKO software (Scientific ToolKit for OpenSees—2.0.4 (http://www.sera-eu.org/export/sites/sera/home/.galleries/Deliverables/SERA_D2.17_Technical-Reports_final.pdf; Petracca et al. 2017a) was used for modal,

pushover and non-linear dynamic analyses. Table 6 shows the main mechanical parameters used in the model. The above data was inferred from static tests carried out in the SCAM laboratory of the Department of Engineering and Geology of the University of Chieti-Pescara (Bathe 2007). The mechanical parameters for stone, mortar joints and filling material (FM) were used to define the damage-mechanism behaviour of the constitutive law DamageTC3D (https://opensees.berkeley.edu/index.php), with two failure criteria for tension and compression, while the timber beams and the concrete slab were modelled as linear elastic isotropic materials. In Kelley (2003) the authors assumed plane stress elements to simulate a different wall made of masonry blocks and lime mortar with one leaf only, so no significant confinement phenomenon was considered. For that reason, the same homogenized compressive strength was used for both elements to consider (in a simplified way) the confinement in the elements. In the current manuscript the elements are more significantly affected by confinement. Solid brick elements were used with different compressive strengths to better simulate the actual state of confinement. The reported values of the elastic moduli were obtained from the uniaxial tests described in Sect. 2. Although these tests are typically carried out to measure the compression strength only and International Standards prescribe different protocols for assessing the elastic moduli, for the sole purpose of the numerical analyses the elastic moduli were derived from the compressive strengths of the materials. The implicit-explicit integration scheme (Petracca et al. 2022) was used for the non-linear materials, where the resulting response is stepwise linear with a positive-definite tangent stiffness matrix due to the explicit extrapolation of the internal variables. Vertical static loads were applied on the top of the cross-timber beams to simulate the additional masses added on the specimen top (6.5 tons). It was assumed that the central beam carried half of the entire additional masses, and the lateral beams carry a quarter of the vertical load each. The boundary conditions used in the model were: fix contraints on the bottom concrete slab to simulate a rigid connection with the shake table; BeamSolidCoupling constraints on the top of the cross-timber beams to simulate the rigid link between them assuming a reasonable stiff connection thanks to the top additional mass system (Fig. 29b). In the dynamic analyses, Rayleigh damping with initial stiffness was considered with 3% damping at the first two wall frequencies with significant participating mass in the X direction. A structured hexahedral mesh was created with a size optimized to obtain reliable results without compromising the running times.

4.2 Modal analysis

Modal analysis after application of all gravity loads was carried out to compare and match the initial dynamic characteristics of the numerical model with that of the tested wall.

Table 7 Wall numerical (and experimental) model frequencies and periods (first five modes). The modal mass participations factors of the numerical model are reported in () in the last column

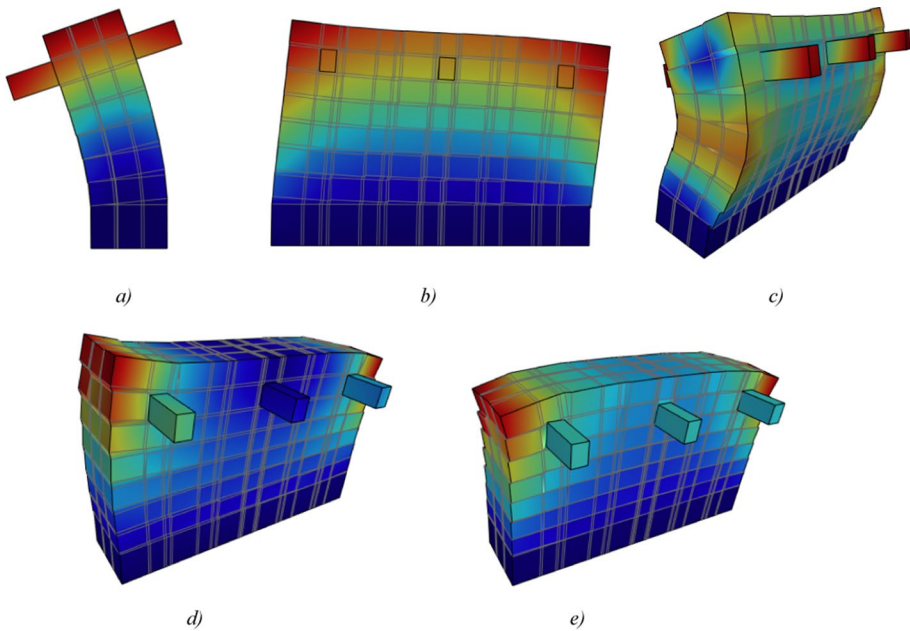| Model	Frequency [Hz]	Period [s]	Direction (mass participation of numerical modes)
Mode 1	2.91(3.12)	0.34 (0.32)	Y (40%)
Mode 2	5.46 (5.45)	0.18 (0.18)	X (53%)
Mode 3	10.73 (9.78)	0.09 (0.10)	Y (17.5%)
Mode 4	10.95 (18.45)	0.09 (0.05)	X (19%)
Mode 5	10.96 (18.45)	0.09 (0.05)	Z (62%)

Fig. 30 Modal deformation of the numerical model for **a** mode 1, **b** mode 2, **c** mode 3, **d** mode 4 and **e** mode 5

Table 7 reports the main frequencies and periods of the tested wall specimen and of its numerical model. A good match is observed for the first three modes. Figure 30 shows the numerical modal main modal shapes.

4.3 Pushover analyses

Static non-linear analyses were carried out to provide an estimate of the in-plane capacity of the walls under equivalent monotonic loading. Displacements were imposed at the master node above the cross-timber beams. The Krylov-Newton algorithm was used for the analyses (Oliver et al. 2008; Knoll and Keyes 2004). Norm displacement increment test with load control was imposed. Tolerance (0.001) and maximum number of iterations (100) were checked for convergence. The unidirectional pushover analysis had 500 increments with adaptive time step up to a displacement of 19 mm (corresponding to a 2.4% drift). A linear function ramp was used for the imposed displacement.

The numerical and experimental pushover curves are reported in Fig. 31 and show a good match in terms of initial stiffness and maximum base shear (around 60 kN). Figure 32 shows the damage propagation during the pushover analysis.

Because the initial stiffness of the monotonic pushover analysis is higher than that of the corresponding dynamic (cyclic) experimental envelope, to evaluate if and how cyclic loading–unloading-reloading affects strength and stiffness, a cyclic pushover analysis was carried out. The cyclic ramp function of Fig. 33 was applied to the imposed displacement with a gradual increase in magnitude and the results are shown in Fig. 34. The reductions in stiffness and strength after the peak in the cyclic analysis clearly indicate how the wall

Fig. 31 Base shear versus displacement results of the experimental (red line) and numerical results (black line) for the wall specimen
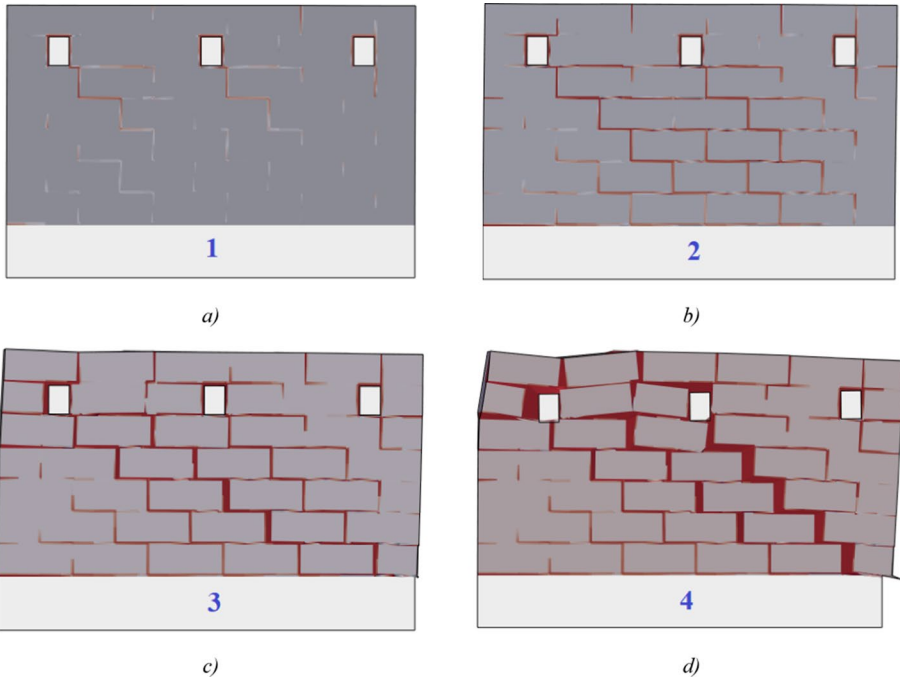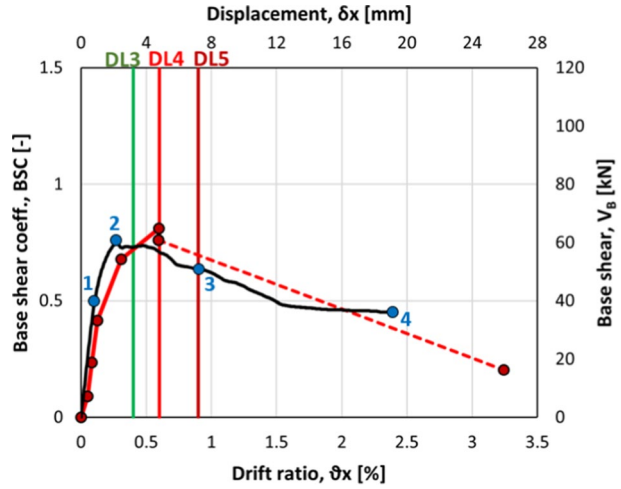

Fig. 32 Material damage and cracking at different stages of the pushover analysis (numbering corresponds to the labels in Fig. 31): **a** at the end of the elastic stage; **b** at peak; **c** during the softening stage and **d** at the end of the analysis

gradually damages following the peak. Figure 35 shows the damage propagation during the cyclic pushover simulation at the steps indicated in the caption. The diagonal cracks are similar to those of Fig. 32, particularly for the diagonal crack below the central timber beam (at an angle of approximately $-45°$ for a force in the positive direction). In the cyclic

Fig. 33 Imposed cyclic displacements imposed at the wall top vs number of increments
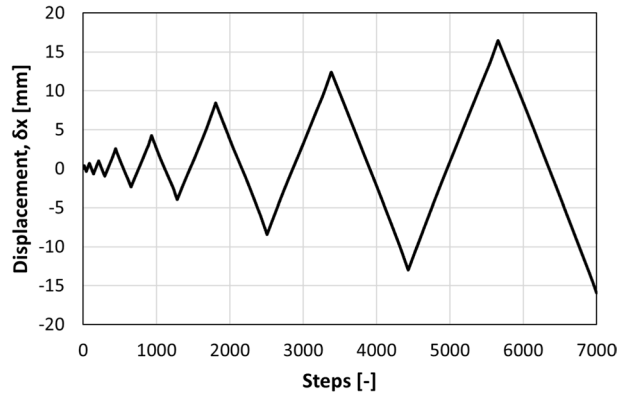
Fig. 34 Base shear vs displacement results of monotonic (black line) and cyclic (gray line) pushover analyses compared with the experimental results (red line)
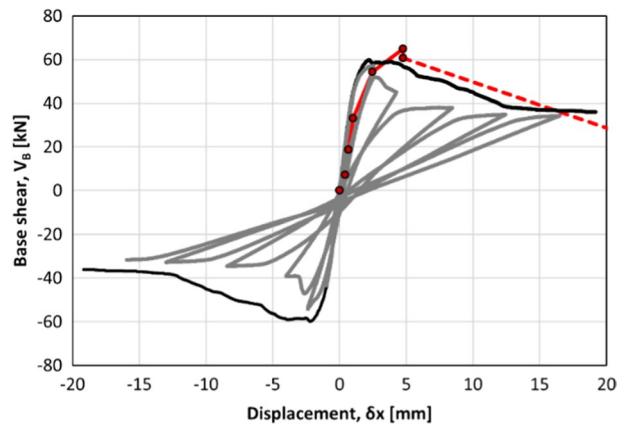
simulation, an additional crack at approximately 45° forms when the specimen is pushed in the negative direction. The crack pattern of the cyclic simulation is consistent with that observed during the experiment.

4.4 Parametric pushover analyses

Parametric monotonic pushover analyses were then carried out to check the main parameters affecting the capacity curve obtained with the micro-model. Pivotal parameters were changed one at a time to highlight the parameters that influence the response of the wall the most, mainly: compressive strength fc, tensile strength ft, Young's modulus E and the material parameter m. The materials considered in the parametric analyses were the mortar and the infill material, as they are the most flexible and least-resistant wall components. The stone units are assumed not to affect the response of the wall as no stone damage was observed during the experiments. Figure 36 shows the pushover curves for different parametric analyses. For each graph the black curve is the original pushover curve of Fig. 31. The results show an increase in the peak strength when the compressive strength of the mortar is increased, while the compressive strength of the infill material has no significant impact on the pushover curves. The fracture energy in compression was kept constant during the parametric studies. An increase in the tensile strength for both materials has a
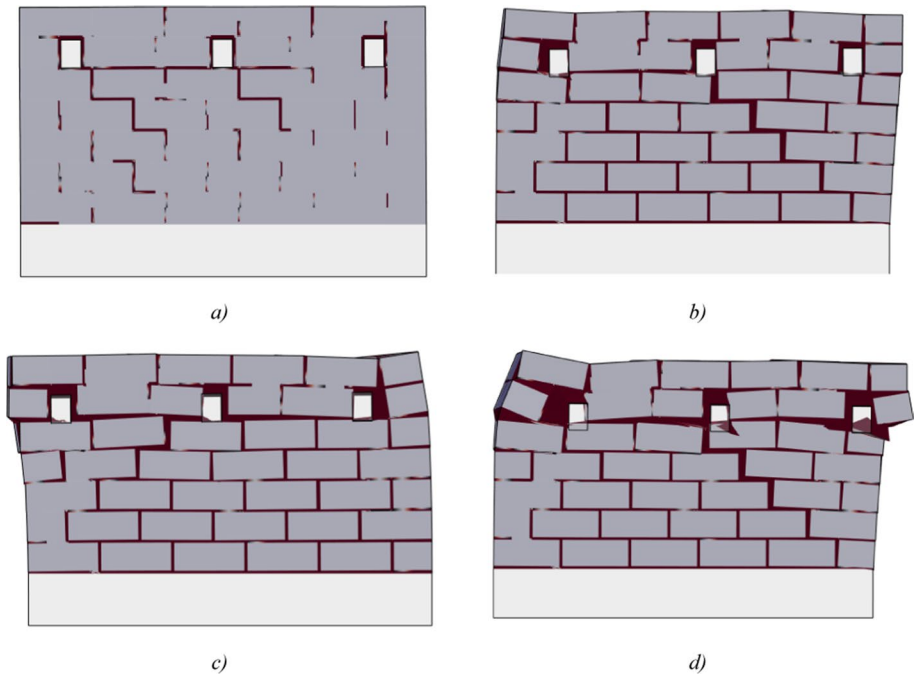
Fig. 35 Material damage and cracking at different steps of the cyclic pushover analysis: **a** step 250; **b** step 1000; **c** step 1300; **d** step 1800 (steps refer to Fig. 33)

significant impact on the wall response, particularly for the infill, as inferred from Fig. 36c, d. The variation of the Young's modulus E for mortar joints has a minor impact on the wall initial stiffness, while an increase in E of the filling material greatly increases the strength of the wall. Lastly, the material parameter m was considered in parametric analyses. It controls the influence that the compressive criterion has on the dilatant behaviour of the model and ranges from 0 to 1. A value of 0 leads to the Drucker-Prager criterion, while a value of 1 leads to the Lubliner criterion (Kelley 2003). The parameter m alters the softening stage, particularly for the infill material where the expansion phenomena are important as this material is confined by the two external leaves. An increase in m leads to a more pronounced softening.

4.5 Non-linear dynamic analyses

Non-linear dynamic analyses were also carried out to complete the calibration of the numerical model with respect to the experimental tests. Two groups of parameters required adjustments as little or no experimental data was available: the mechanical characteristics of the FM and the values of the fracture energy in tension for the infill and for the mortar. The values of the FM mechanical characteristics were assumed based on a range of possible values calibrated in sensitivity analyses. Similarly to the pushover analyses the Krylov-Newton algorithm, Penalty method constraints, and norm displacement increment test were used. The integrator object used was TRBDF2 (Petracca et al. 2017b; Bank et al. 1985), a mixed scheme that alternates between the Trapezoidal scheme and a 3-point backward
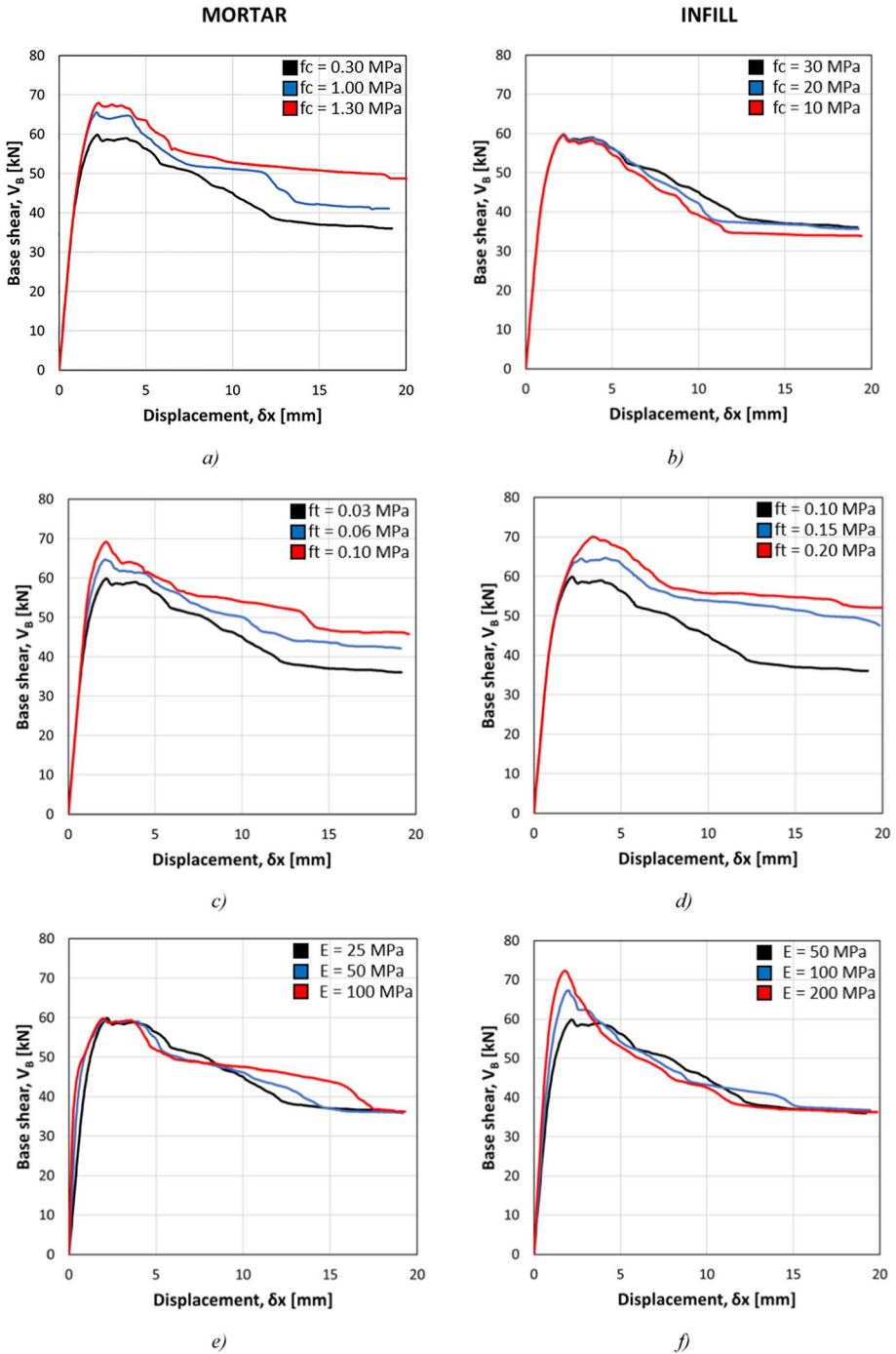
Fig. 36 Parametric results of monotonic pushover analyses with varying **a** mortar fc; **b** fc infill; **c** mortar ft; **d** infill ft; **e** mortar E; **f** infill E; **g** mortar m and **h** infill m
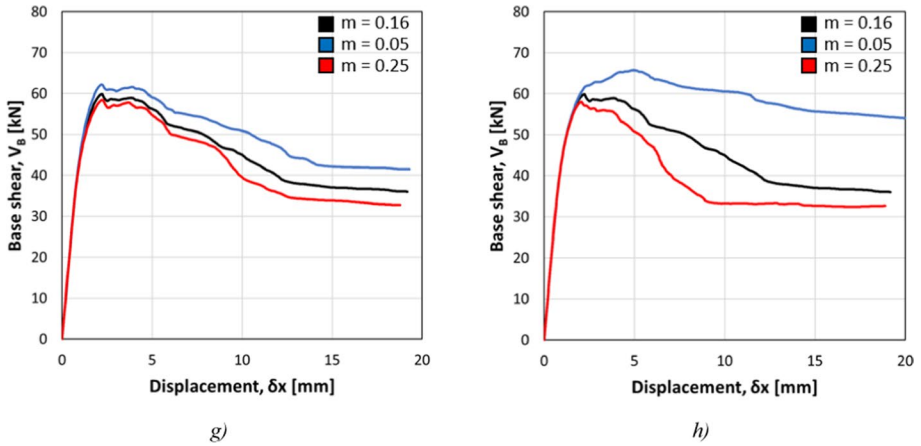
g)

h)

Fig. 36 (continued)

Euler scheme. It does this to conserve energy and momentum, something the Newmark method does not always guarantee.

The horizontal seismic input for the first dynamic analysis was the 100% scale earthquake recorded on the shake table test of the experimental campaign with nominal horizontal PGA of 0.70 g. The time step of the input signal is dt=0.0066 s. The analysis was carried out with 13,000 increments with fixed time step for a total of 13 s. The time step of the post-processor results is dt=0.001 s, a good compromise between computational times and accuracy of the results. Figure 37 reports the results of the displacement demand and the base shear during the seismic simulation. At approximately 6 s the model reached the peak strength of about 50 kN for a top displacement of 6–7 mm, similarly to the experimental dynamic test. After reaching the base shear peak the main frequency clearly shortens and the displacement demand increases.

a)

b)
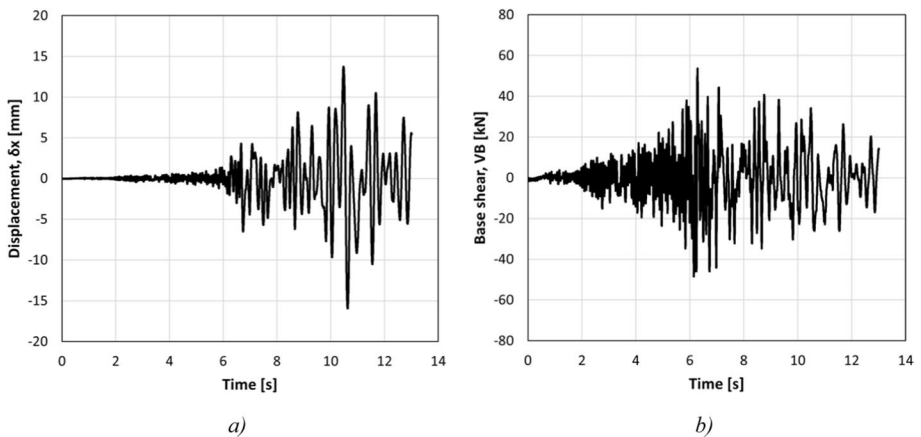
Fig. 37 Time histories of: **a** wall top displacement response and **b** base shear (Input is 100% of horizontal component of the Gazli ground motion as recorded on the shake table turing the experimental tests)

Fig. 38 Base shear vs displacement results for dynamic analysis at 100% scale of the selected ground motion (red line) and comparison with the same results for unidirectional (black line) and cyclic (blue line) pushover analyses
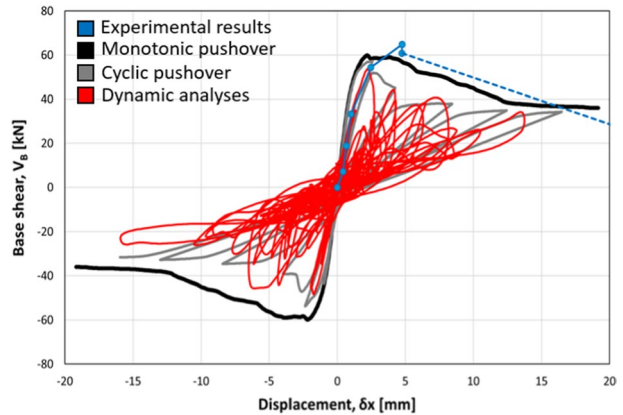

Figure 38 reports the hysteretic curve of the dynamic analyses. The numerical dynamic test red curve shows a good match with the results of the pushover analyses (monotonic and cyclic) in terms of initial stiffness, strength and displacement demand. The strength reached with the dynamic analysis is lower than the peaks obtained with the pushover analyses (monotonic and cyclic) because of more random cyclical actions and cyclic damage. The final pattern of the specimen damage corresponds to the mechanisms activated and observed during the experimental tests. Shear diagonal cracks are clearly visible in Fig. 39.

5 Summary and conclusions

This paper presents and discusses the results of a series of sequential tests carried out on a three-leaf masonry wall (representative of older masonry building walls found in earthquake prone regions in several Mediterranean countries) on the shaking table of the University of Bristol within the framework of the EU-funded SERIES research initiative. Numerical simulations are also presented to validate the corresponding experimental results. The tested wall, designed to be representative of a wall in the top floor of a masonry building, had two outer leaves made of regular stones and an inner weaker
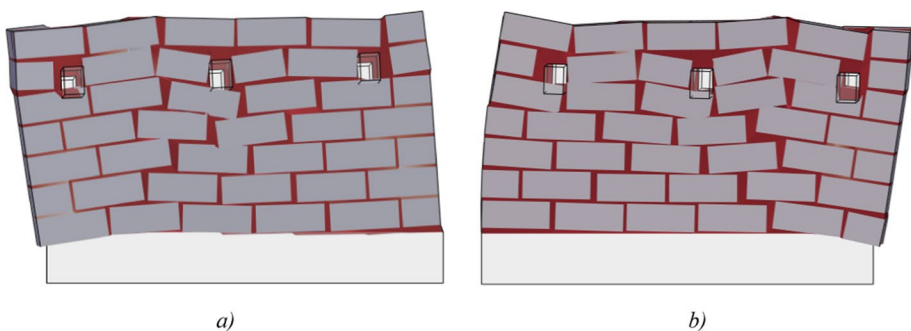

Fig. 39 Maximum Damage and crack patterns during non-linear dynamic analysis in **a** − X and **b** + X direction

infill representative of infills where lose material was bound together by a weak mortar. The stones were connected by a special mortar whose components were selected to reproduce the low mechanical properties that are typically found in old masonry buildings. An additional mass was added to the wall top to represent the weight of the roof carried by the wall. The wall was designed to fail in shear. A white noise test preceded the dynamic tests to characterize the initial dynamic properties of the wall. The wall was subjected to a sequence of horizontal ground motions, all obtained from the same acceleration record scaled by scale factors from 10% up to 140%.

The shaking table tests main results can be summarized as follows:

- No damage was observed in the stones. Damage concentrated in the "weaker" links, i.e. the mortar and the infills;
- The main resisting mechanisms and damage patterns under increasing dynamic ground accelerations were identified, showing shear failure (predicated in the wall design phase), but also lateral instability and detachment of the outer leaves;
- The above mechanisms are influenced by the presence of the inner, weaker core. Early failure of the loose material that forms the infills and lateral expansion due to Poisson effects initiate out-of-plane bending of the outer leaves;
- The drifts corresponding to the attainments of three damage limit states defined by the technical document CNR-DT 212 (2013) were compared with results of the test sequence on the wall. A good match was found between drift limits provided by the above code for brittle (shear deficient) walls and observed damage;
- The results show that the test sequence would have benefitted from an additional test between the 100% and 140% tests. The specimen reached the ultimate state (or DL4) for the 100% scaled records and the 140% scaled record lead to complete failure with large maximum and residual lateral drifts way beyond DL5 (that can be assimilated to the collapse limit state);
- Post processing of the recorded results indicated that in some cases the recorded output contained spurious data that derived from the frequencies of higher modes. As damage increases, the wall becomes highly discontinuous with stone blocks that detach from the mortar and move, rotate as rigid bodies. The as-recorded data was "cleaned" with an appropriate filter to yield a signal containing the wall frequencies and accelerations associated with the longitudinal vibrations only;
- The experimental results confirmed the predictions provided by design codes, such as CNR-DT 212 (2013). Three-leaf masonry walls are highly vulnerable to ground motions by showing not only in-plane failures (shear in the present case), but also out-of-plane bending mechanisms. Reinforcement of such structural system is necessary to increase the in-plane strength and prevent the out-of-plane bending;
- Funding constraints limited the number of tested specimens to one, instead of the three identical specimens originally planned. Additional specimens would have allowed a statistical evaluation of the wall response and different ground motions with different energy and frequency contents could have been used.

Numerical simulations complement the experimental analyses to both validate the experimental results and assess how well advanced modelling techniques can describe the complex response of brittle walls. The results of pushover (both monotonic and cyclic) and dynamic analyses are commented hereafter:

- Modal analysis was used to calibrate the initial elastic properties of the constitutive materials by comparing the initial dynamic characteristics of the numerical model with those of the tested wall;
- Nonlinear monotonic and cyclic pushover analyses show a good match with the experimental results in terms of initial stiffness, strength and displacements/drifts;
- Parametric analyses were carried out to identify the main parameters affecting the capacity curve obtained with the pushover analysis. The parameters that affect the results the most are: the compressive strength of the mortar, the tensile strength of both mortar and infill, the E modulus of the infill, the shear-compression reduction factor of the infill;
- The force–displacement curves (Fig. 38) and the damage patterns (among others Table 4, Figs. 35 and 39) show a satisfactory match between experimental dynamic tests and numerical analyses of the wall specimen in terms of base shear–displacement responses and damage patterns.
- The numerical model analyses were fast and relatively stable. Once the material parameters were adjusted, convergence was reached in all reported cases. The numerical models can be used in the future to further explore the behaviour of these brittle walls by changing, for example, the input ground motion or by simulating different strengthening techniques. Numerical analyses can shed light on cases where data recording failed during the test. Also, the softening stage of the wall behaviour can be traced with numerical analyses while it could not be traced during the experimental tests that were basically force-controlled procedures for the wall.

Additional vulnerability of the studied wall derives from the effects of the vertical component of the ground motion, particularly for near fault events. Experimental tests on a similar walls with the same horizontal ground motion and including the vertical component were carried out within the same research project (Brando et al. 2022). These will be described in publications that are under preparation.

Data availability All experimental data is available upon request.

Declarations

Conflict of interest The authors have not disclosed any competing interests.

References

Augenti N, Parisi F (2010) Learning from construction failures due to the 2009 L'Aquila, Italy, earthquake. J Perform Constr Facil 24(6):536–555. https://doi.org/10.1061/(ASCE)CF.1943-5509.0000122

Bank RE, Coughran WM, Fichter W, Grosse EH, Rose DJ, Smith RK (1985) Transient simulations of silicon devices and circuits. IEE Trans CAD 4:436–451

Bathe KJ (2007) Conserving energy and momentum in nonlinear dynamics: a simple impicit time integration scheme. Comput Struct 85:437–445. https://doi.org/10.1016/j.compstruc.2006.09.004

Binda L, Pina-Henriques J, Anzani A, Fontana A, Lourenço PB (2006) A contribution for the understanding of load-transfer mechanisms in multi-leaf masonry walls: testing and modelling. Eng Struct 28(8):1132–1148. https://doi.org/10.1016/j.engstruct.2005.12.004

Boore DM, Joyner WB (1982) The empirical prediction of ground motion. Bull Seismol Soc Am 72(6):43–60

Borri A (2010) Costruzioni storiche e qualità muraria: problematiche e possibili interventi di consolidamento. In: Italian national conference of "sicurezza e conservazione nel recupero dei beni culturali colpiti da sisma" (Italian), Venice

Brando G, Criber E, De Matteis G (2015) The effects of L'aquila earthquake on the St. Gemma church in Goriano Sicoli: part II—fem analysis. Bull Earthq Eng 13(12):3733–3748. https://doi.org/10.1007/s10518-015-9793-3

Brando G, De Matteis G, Spacone E (2017) Predictive model for the seismic vulnerability assessment of small historic centres: application to the inner Abruzzi Region in Italy. Eng Struct 153:81–96. https://doi.org/10.1016/j.engstruct.2017.10.013

Brando G, Cianchino G, Rapone D, Spacone E, Biondi S (2021) A CARTIS-based method for the rapid seismic vulnerability assessment of minor Italian historical centres. Int J Disaster Risk Reduct. https://doi.org/10.1016/j.ijdrr.2021.102478

Brando G, Vacca G, Di Michele F, Capasso I, Spacone E (2022) Experimental and numerical mechanical characterization of unreinforced and reinforced masonry elements with weak air lime mortar joints. Sustainability 14(7):3990. https://doi.org/10.3390/su14073990

Cascardi A, Leone M, Aiello MA (2020) Transversal joining of multi-leaf masonry through different types of connector: experimental and theoretical investigation. Constr Build Mater 265:120733. https://doi.org/10.1016/j.conbuildmat.2020.120733

Casolo S, Milani G (2013) Simplified out-of-plane modelling of three-leaf masonry walls accounting for the material texture. Constr Build Mater 40:330–351. https://doi.org/10.1016/j.conbuildmat.2012.09.090

Circolare 21 Gennaio (2019) n. 7 C.S.LL.PP "Istruzioni per l'applicazione dell'Aggiornamento delle Norme Tecniche per le Costruzioni, di cui al decreto ministeriale 17 gennaio 2018" (in Italian)

CNR (2014) Commissione di studio per la predisposizione e l'analisi di norme tecniche relative alle costruzioni. Istruzioni per la Valutazione Affidabilistica della Sicurezza Sismica di Edifici Esistenti CNR-DT 212/2013, p 190

Cocco G, D'Aloisio A, Spacone E, Brando G (2019) Seismic vulnerability of buildings in historic centers: from the "urban" to the "aggregate" scale. Front Built Environ. https://doi.org/10.3389/fbuil.2019.00078

de Carvalho Bello CB, Boscato G, Meroi E, Cecchi A (2020) Non-linear continuous model for three leaf masonry walls. Constr Build Mater 244:118356. https://doi.org/10.1016/j.conbuildmat.2020.118356

De Matteis G, Brando G, Corlito V (2019) Predictive model for seismic vulnerability assessment of churches based on the 2009 L'Aquila earthquake. Bull Earthq Eng. https://doi.org/10.1007/s10518-019-00656-7

Derakhshan H, Griffith MC, Ingham JM (2013) Airbag testing of multi-leaf unreinforced masonry walls subjected to one-way bending. Eng Struct 57:512–522. https://doi.org/10.1016/j.engstruct.2013.10.006

Di Michele F (2022) Shake table tests of as-built and strengthened three-leaf masonry walls. PhD Thesis, 2022, Department of Engineering and Geology, University G. d'Annunzio of Chieti-Pescara, Italy

Di Michele F, Cantagallo C, Spacone E (2020) Effects of the vertical seismic component on seismic performance of an unreinforced masonry structures. Bull Earthq Eng 18(4):1635–1656. https://doi.org/10.1007/s10518-019-00765-3

Di Michele F, Spacone E, Camata G, Brando G et al (2021) Project #12—REBOND—REsponse of as-built and strengthened three-leaf masONry walls by dynamic tests. In: D10.1—digital proceedings on SERA transnational access activities

Dihoru L et al (2019) A computer vision approach for dynamic tracking of components in a nuclear reactor core model. Nucl Eng Des 344:1–14. https://doi.org/10.1016/j.nucengdes.2019.01.017

Egermann R, Neuwald-Burg C (1994) Assessment of the load bearing capacity of historic multiple leaf masonry walls. In: Proceedings of the 10th international brick/block masonry conference, pp 1603–1612

EN 1015-11 (2019) Methods of test for mortar for masonry—part 11: determination of flexural and compressive strength of hardened mortar

Giaretton M, Valluzzi MR, Mazzon N, Modena C (2017) Out-of-plane shake-table tests of strengthened multi-leaf stone masonry walls. Bull Earthq Eng 15(10):4299–4317. https://doi.org/10.1007/s10518-017-0125-7

http://www.sera-eu.org/export/sites/sera/home/.galleries/Deliverables/SERA_D2.17_Technical-Reports_final.pdf

Kelley CT (2003) Solving nonlinear equations with Newton's method, SIAM

Knoll DA, Keyes DE (2004) Jacobian-free Newton–Krylov methods: a survey of approaches and applications. J Comput Phys 193:357–397

Luco JE, Ozcelik O, Conte JP (2010) Acceleration tracking performance of the UCSD-NEES shake table. J Struct Eng 136(5):481–490. https://doi.org/10.1061/(ASCE)ST.1943-541X.0000137

Magenes G, Penna A, Senaldi IE, Rota M, Galasco A (2014) Shaking table test of a strengthened full-scale stone masonry building with flexible diaphragms. Int J Archit Herit 8(3):349–375. https://doi.org/10.1080/15583058.2013.826299

Manos GC (2020) Personal communication. Aristotle University of Thessaloniki, Greece

Moaveni B, Stavridis A, Lombaert G, Conte JP, Shing PB (2013) Finite-element model updating for assessment of progressive damage in a 3-story infilled RC frame. J Struct Eng (united States) 139(10):1665–1674. https://doi.org/10.1061/(ASCE)ST.1943-541X.0000586

Martínez I, Castillo A, Martínez E, Castellote M (2013) Physico-chemical material characterization of historic unreinforced masonry buildings: the first step for a suitable intervention. Constr Build Mater 40:352–360. https://doi.org/10.1016/j.conbuildmat.2012.09.091

Mazzon N, Chavez CMM, Valluzzi MR, Casarin F, Modena C (2010) Shaking table tests on multi-leaf stone masonry structures: analysis of stiffness decay. Adv Mater Res 133–134:647–652. https://doi.org/10.4028/www.scientific.net/AMR.133-134.647

Mugabo I, Barbosa AR, Sinha A, Higgins C, Riggio M, Pei S, van de Lindt JW, Berman JW (2021) System identification of UCSD-NHERI shake-table test of two-story structure with cross-laminated timber rocking walls. J Struct Eng (united States). https://doi.org/10.1061/(ASCE)ST.1943-541X.0002938

Oliveira DV, Silva RA, Garbin E, Lourenço PB (2012) Strengthening of three-leaf stone masonry walls: an experimental research. Mater Struct Constr 45(8):1259–1276. https://doi.org/10.1617/s11527-012-9832-3

Oliver J, Huespe AE, Cante JC (2008) An implicit/explicit integration scheme to increase computability of nonlinear material and contact/friction problems. Comput Methods Appl Mech Eng 197(21–24):1865–1889

Open System for Earthquake Engineering Simulation (OpenSees) Softaware. https://opensees.berkeley.edu/index.php

Pappas A (2011) Calibration of the numerical material behaviour of multi-leaf stone masonry walls based on experimental results. Padova (Italy)

Pereira M (2017) Análise dos efeitos do sismo de 9 de julho de 1998 no património religioso dos Açores. Leira

Petracca M, Candeloro F, Camata G (2017a) "STKO user manual". ASDEA software technology, Pescara (Italy). MPCO recorded—written by ASDEA software technology: M. Petracca, G. Camata. https://asdeasoft.net/stko/

Petracca M, Pelà L, Rossi R, Zaghi S, Camata G, Spacone E (2017b) Micro-scale continuous and discrete numerical models for nonlinear analysis of masonry shear walls. Constr Build Mater. https://doi.org/10.1016/j.conbuildmat.2017.05.130

Petracca M, Camata G, Spacone E, Pelà L (2022) Efficient constitutive model for continuous micro-modeling of masonry structures. Int J Archit Herit. https://doi.org/10.1080/15583058.2022.2124133

Ramalho M, Taliercio A, Anzani A, Binda L, Papa E (2005) Experimental and numerical study of multi-leaf masonry walls. Adv Archit Ser 20:333–342

Roselli G et al (2019) Mortar analysis of historic buildings damaged by recent earthquakes in Italy. Eur Phys J plus 134(10):1–14. https://doi.org/10.1140/epjp/i2019-13024-2

Saretta Y, Sbrogiò L, Valluzzi MR (2021) Seismic response of masonry buildings in historical centres struck by the 2016 Central Italy earthquake. Calibration of a vulnerability model for strengthened conditions. Constr Build Mater 299:123911. https://doi.org/10.1016/j.conbuildmat.2021.123911

Schafer RW (2011) What is a Savitzky–Golay filter? IEEE Signal Process Mag 28(4):111–1117

Silva B, Dalla Benetta M, Da Porto F, Modena C (2014) Experimental assessment of in-plane behaviour of three-leaf stone masonry walls. Constr Build Mater 53:149–161. https://doi.org/10.1016/j.conbuildmat.2013.11.084

Turnšek, V, Čačovič F (1971) Some experimental results on the strength of brick masonry walls. In: Proceedings of the 2nd international brick masonry conference, pp 149–156

UNI-Ente Italiano di Normazione (1926) Metodi di prova per pietre naturali—determinazione della resistenza a compressione uniassiale-UNI EN 1926:2007. 200AD (in Italian)

Vintzileou E (2011) Three-leaf masonry in compression, before and after grouting: a review of literature. Int J Archit Herit 5(4–5):513–538. https://doi.org/10.1080/15583058.2011.557137

Vintzileou E, Tassios TP (1995) Three-leaf stone masonry strengthened by injecting cement grouts. J Struct Eng (united States) 121(5):848–856. https://doi.org/10.1061/(ASCE)0733-9445(1995)121:5(848)

Authors and Affiliations

Francesco Di Michele[1] · Enrico Spacone[1] · Guido Camata[1] · Giuseppe Brando[1] · Anastasios Sextos[2,5] · Adam Crewe[2] · George Mylonakis[2,4] · Matt Diez[2] · Luiza Dihoru[2] · Humberto Varum[3]

✉ Enrico Spacone
  enrico.spacone@unich.it

1 Department of Engineering and Geology, University "G. d'Annunzio" of Chieti-Pescara, Viale Pindaro 42, 65127 Pescara, Italy

2 Department of Civil Engineering, University of Bristol, Bristol, UK

3 CONSTRUCT-LESE, Faculty of Engineering, University of Porto, Porto, Portugal

4 Department of Civil Infrastructure and Environmental Engineering, Khalifa University, Abu Dhabi, UAE

5 Department of Civil Engineering, National Technical University of Athens, Athens, Greece